

NAVAL POSTGRADUATE SCHOOL
Monterey, California



THESIS

**REMOTE MEASUREMENT OF AEROSOL OPTICAL PROPERTIES
USING THE NOAA POES AVHRR AND GOES IMAGER DURING
TARFOX**

by

Brian B. Brown

June 1997

Thesis Advisor:

Co-Advisor:

Philip A. Durkee

Carlyle H. Wash

Approved for public release; distribution is unlimited.

DTIC QUALITY INSPECTED 8

19971027 037

REPRODUCTION QUALITY NOTICE

This document is the best quality available. The copy furnished to DTIC contained pages that may have the following quality problems:

- **Pages smaller or larger than normal.**
- **Pages with background color or light colored printing.**
- **Pages with small type or poor printing; and or**
- **Pages with continuous tone material or color photographs.**

Due to various output media available these conditions may or may not cause poor legibility in the microfiche or hardcopy output you receive.



If this block is checked, the copy furnished to DTIC contained pages with color printing, that when reproduced in Black and White, may change detail of the original copy.

REPORT DOCUMENTATION PAGE			Form Approved OMB No. 0704-0188	
Public reporting burden for this collection of information is estimated to average 1 hour per response, including the time for reviewing instructions, searching existing sources, gathering and maintaining the data needed, and completing and reviewing the collection of information. Send comments regarding this burden estimate or any other aspect of this collection of information, including suggestions for reducing this burden to Washington Headquarters Services, Directorate for Information Operations and Reports, 1215 Jefferson Davis Highway Suite 1204, Arlington, VA 22202-4312, and to the Office of Management and Budget, Paperwork Reduction Project (0704-0188), Washington, DC 20503.				
1. AGENCY USE ONLY (Leave blank)	2. REPORT DATE June 1997	3. REPORT TYPE AND DATES COVERED Master's Thesis		
4. TITLE AND SUBTITLE REMOTE MEASUREMENT OF AEROSOL OPTICAL PROPERTIES USING THE NOAA POES AVHRR AND GOES IMAGER DURING TARFOX			5. FUNDING NUMBERS	
6. AUTHOR(S) Brian B. Brown				
7. PERFORMING ORGANIZATION NAME(S) AND ADDRESS(ES) Naval Postgraduate School Monterey, CA 93943-5000			8. PERFORMING ORGANIZATION REPORT NUMBER	
9. SPONSORING/MONITORING AGENCY NAME(S) AND ADDRESS(ES)			10. SPONSORING/MONITORING AGENCY REPORT NUMBER	
11. SUPPLEMENTARY NOTES The views expressed in this thesis are those of the author and do not reflect the official policy or position of the Department of Defense or the U.S. Government.				
12a. DISTRIBUTION/AVAILABILITY STATEMENT Approved for public release; distribution is unlimited.			12b. DISTRIBUTION CODE	
13. ABSTRACT (Maximum 200 words) A radiative transfer algorithm in the solar wavelengths for the NOAA POES AVHRR and GOES Imager is proposed for the cloud-free, marine atmosphere. The algorithm combines linearized, single-scattering theory with an estimate of bi-directional surface reflectance. Phase functions are parameterized using an aerosol distribution model and the ratio of radiance values measured in channels 1 and 2 of the AVHRR. Retrieved satellite aerosol optical depth is compared to airborne sunphotometer data and derived values from particle size distributions collected during the Tropospheric Aerosol Radiative Forcing Observational Experiment (TARFOX) in July 1996. Error in the satellite derived values from the AVHRR originates in error in modeling aerosol size distributions, corresponding phase function parameterization and treatment of specular surface reflectance. Extension of the algorithm to the GOES Imager provided results consistent with the AVHRR.				
14. SUBJECT TERMS Radiative transfer, NOAA AVHRR, GOES, aerosol optical depth, TARFOX			15. NUMBER OF PAGES 84	
			16. PRICE CODE	
17. SECURITY CLASSIFICATION OF REPORT Unclassified	18. SECURITY CLASSIFICATION OF THIS PAGE Unclassified	18. SECURITY CLASSIFICATION OF ABSTRACT Unclassified	20. LIMITATION OF ABSTRACT UL	

NSN 7540-01-280-5500

Standard Form 298 (Rev 2-89)
Prescribed by ANSI Std. Z39-18
298-102

Approved for public release; distribution is unlimited

REMOTE MEASUREMENT OF AEROSOL OPTICAL PROPERTIES
USING THE NOAA POES AVHRR AND GOES IMAGER DURING
TARFOX

Brian B. Brown
Lieutenant Commander, United States Navy
B.S., United States Naval Academy, 1986

Submitted in partial fulfillment of the
requirements for the degree of

MASTER OF SCIENCE IN METEOROLOGY AND
PHYSICAL OCEANOGRAPHY


from the

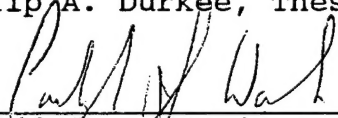
NAVAL POSTGRADUATE SCHOOL
JUNE 1997

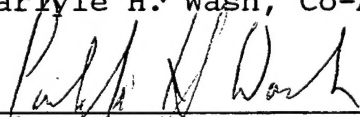
Author:


Brian B. Brown

Approved by:


Philip A. Durkee, Thesis Advisor


Carlyle H. Wash, Co-Advisor


Carlyle H. Wash, Chairman
Department of Meteorology

DAIC QUALITY INSPECTED 3

ABSTRACT

A radiative transfer algorithm in the solar wavelengths for the NOAA POES AVHRR and GOES Imager is proposed for the cloud-free, marine atmosphere. The algorithm combines linearized, single-scattering theory with an estimate of bi-directional surface reflectance. Phase functions are parameterized using an aerosol distribution model and the ratio of radiance values measured in channels 1 and 2 of the AVHRR. Retrieved satellite aerosol optical depth is compared to airborne sunphotometer data and values derived from aerosol particle size distributions collected during the Tropospheric Aerosol Radiative Forcing Observational Experiment (TARFOX) in July 1996. Error in the satellite derived values from the AVHRR originates in error in modeling aerosol size distributions, corresponding phase function parameterization and treatment of specular surface reflectance. Extension of the algorithm to the GOES Imager provided results consistent with the AVHRR.

TABLE OF CONTENTS

I.	INTRODUCTION	1
II.	RADIATIVE TRANSFER THEORY	5
A.	EXTINCTION, SCATTERING, AND OPTICAL DEPTH	5
B.	RADIATIVE TRANSFER SOLUTION	7
1.	Aerosol Radiance (I_a)	9
2.	Scattering Phase Function (P)	11
III.	DATA	15
A.	TARFOX DATA SETS	15
B.	INSTRUMENTS	16
1.	NOAA Advanced Very High Resolution Radiometer (AVHRR)	16
2.	GOES Imager	17
3.	NASA AMES Airborne Autotracking Sunphotometer	18
4.	Passive Cavity Aerosol Spectrometer Probe (PCASP)	19
5.	Particle Soot Absorption Photometer (PSAP)	20
IV.	OPTICAL DEPTH RETRIEVAL PROCEDURES	21
A.	SATELLITE IMAGE RETRIEVAL/DISPLAY	21
B.	OPTICAL DEPTH RETRIEVAL	21
C.	RADIATIVE TRANSFER CODE	22
1.	Solar Irradiance/Solar Radiance	22
2.	Ozone and Rayleigh Optical Depths	23
3.	Scattering Phase Function	23
a.	NOAA/NESDIS Derived Scattering Phase Function	24
b.	Particle Size Parameter (S_{12}) Derived Scattering Phase Functions ..	24
V.	RESULTS	33
A.	OVERVIEW OF TARFOX	33
B.	25 JULY 1996	34
1.	Weather	34
2.	Absorption	35
3.	Water Vapor	36
4.	Aerosol Distributions/Phase Functions	36
a.	25 July Intercomparisons	36
b.	21, 25, and 27 July Intercomparisons	38
5.	NOAA 14 Aerosol Optical Depth Retrieval ..	39
6.	GOES 8 Aerosol Optical Depth Retrievals ..	41
C.	18 JULY 1996	43
1.	Weather	43
2.	NOAA 14 Aerosol Optical Depth Retrieval ..	43
D.	16 JULY 1996	44
1.	Weather	44
2.	NOAA 14 Aerosol Optical Depth Retrieval ..	44

E.	23 JULY 1996	45
1.	Weather	45
2.	NOAA 14 Aerosol Optical Depth Retrieval ..	45
VI.	CONCLUSIONS/RECOMMENDATIONS	67
A.	CONCLUSIONS	67
B.	RECOMMENDATIONS	69
	LIST OF REFERENCES	71
	INITIAL DISTRIBUTION LIST	73

ACKNOWLEDGEMENTS

I would like to thank my advisors, Dr. Philip A. Durkee and Dr. Carlyle H. Wash of the Department of Meteorology, Naval Postgraduate School, for their guidance and support during the development of this thesis. Additionally, I owe a debt of gratitude to Mr. Kurt Nielsen of the NPS Remote Sensing Laboratory for the computer assistance provided, especially with the UNIX operating system and FORTRAN. Kurt never failed to provide immediate support as the System Administrator for the NPS remote sensing skunkworks.

My most sincere thank you to Mr. Pepijn Veefkind of the Physics and Electronics Laboratory (FEL), Netherlands Organization of Applied Scientific Research (TNO), the Hague, the Netherlands. Without his hands on assistance, much of this thesis could not have been completed. At every potential dead end, he always came up with a fresh idea or direction to pursue. For this I will be forever grateful.

I would also like to thank the scientific teams at the University of Washington, United Kingdom Meteorological Research Facility, NOAA/NESDIS Satellite Research Laboratory, and NASA AMES for their contributions to the data used in this study.

I. INTRODUCTION

Atmospheric aerosols play a major role in the Earth's radiation budget. Aerosols contribute to both a direct and indirect change in the Earth's albedo which may lead to changes in the heating of the Earth and its atmosphere. Variations in natural and anthropogenic aerosols directly alter the scattering of incoming shortwave radiation to space. Particles that become cloud condensation nuclei create variations in local cloud characteristics which indirectly affect solar insolation. Charlson et al. (1992) report that shortwave radiative forcing of the Earth's climate due to an estimated increase in anthropogenic sulfate optical depth of 0.04 is enough to offset longwave forcing by greenhouse gases. Recent research efforts have focused on anthropogenic sources of aerosols in coastal regions and their radiative effect on the Earth's climate.

For the U.S. Navy, characterization of aerosol radiative properties in the coastal zone is important to the design, planning, and operation of electro-optical weapons and sensor systems near coastal boundaries. Aerosols scatter and degrade electro-optical system performance by scattering visible and near-infrared energy used by these systems.

In situ measurements of both aerosol radiative and size distribution characteristics using instruments such as sunphotometers, spectrometers, and radiometers, provide highly accurate, but spatially and temporally limited measurements. Satellite radiometers offer an alternative method to measure aerosol radiative effects that cover large areas.

To be useful for this purpose, a satellite radiometer must possess high spatial and radiometric resolution in its visible and/or near-infrared channels. Until recently, the only operational U.S. satellite system with fine enough spatial and digital resolution to indirectly measure aerosol radiative properties was the NOAA Advanced Very High Resolution Radiometer (AVHRR) carried aboard the NOAA Polar-orbiting Operational Environmental Satellites (POES). With the POES series satellites, retrievals are limited to one or two passes per day over a given mid latitude area due to the nature of the polar orbit. Starting in late 1994, NOAA launched a series of two new geostationary weather satellites, the Geostationary Operational Environmental Satellites or GOES. GOES included an improved visible spectrum radiometer (GOES Imager) with similar radiometric resolution to the AVHRR. The primary advantage of the GOES series radiometer is its capability of imaging an area approximately every 15 minutes. This enhanced temporal resolution potentially offers insight into short-term, large-scale aerosol variations previously not available.

Most of the satellite aerosol retrieval techniques to date have focused on the AVHRR. Unique to the AVHRR among operational meteorological satellites is a two solar channel capability that allows better characterization of phase scattering effects; this capability is not available using the single solar channel GOES Imager. Earlier work by Durkee et al. (1991) and Rouault and Durkee (1992) exploits this capability of the AVHRR and provides the basic framework for the aerosol retrieval technique used in this study.

Until recently, the ability to validate optical depth retrieval results has been limited by the lack of field data to provide closure on comparable measurements. In July

1996, the Tropospheric Aerosol Radiative Forcing Observational Experiment (TARFOX) was conducted to attempt to provide this closure.

The objectives of this thesis are threefold:

- Develop an improved linearized, single-scattering atmospheric aerosol optical depth retrieval algorithm for use by both NOAA POES AVHRR and GOES Imager systems based on the approach of Durkee *et al.* (1991).

- Validate aerosol optical depth retrievals using TARFOX field observations of optical depth and aerosol size distributions.

- Demonstrate temporal utility of GOES aerosol optical depth retrievals.

Chapter II describes the basic radiative transfer theory used in the satellite optical depth retrievals. Chapter III outlines the TARFOX data set and basic instrumentation used. Chapter IV describes aerosol optical depth retrieval procedures. Chapter IV provides results. Chapter VI discusses final conclusions and recommendations.

II. RADIATIVE TRANSFER THEORY

Radiative transfer theory provides the basis for methods used to characterize aerosol properties from satellite remote measurement (see Liou, 1980, for a complete treatment of the theory). In a cloud-free, marine environment, the shortwave, solar radiation measured by a satellite radiometer is primarily the result of scattering by both the molecular constituents of the atmosphere (Rayleigh scattering) and larger suspended aerosol (Mie scattering). Absorption plays a small role in the attenuation of incoming solar radiation in the visible (0.4-0.7 μm) and near-infrared (NIR) spectrums (0.7-0.9 μm). Corrections to solar irradiance of less than 5% for ozone absorption in the upper atmosphere are applied; aerosols are assumed to be non-absorbing. At some solar wavelengths, corrections for water vapor absorption on the order of 2-3% of measured radiance are also applied. In the absence of Sun glint, reflectance from the ocean surface is also small. Contributions to satellite measured radiance due to sea surface foam and subsurface reflectance can be accounted for with empirical measurements. Specular reflectance is estimated using Fresnel coefficients. Figure 2.1 illustrates this radiative transfer process. This chapter describes the basic theory used in the methods employed by this study to obtain aerosol optical properties. All further discussion pertains to radiative transfer in a cloud-free, marine environment.

A. EXTINCTION, SCATTERING, AND OPTICAL DEPTH

Radiative extinction includes both scattering and absorption by atmospheric constituents; extinction is highly

wavelength dependent. Equation 2.1 defines the extinction coefficient:

$$\sigma_{\text{ext}} = \int_0^{\infty} \pi r^2 Q_{\text{ext}}(m, r) n(r) dr \quad (2.1)$$

where r is particle radius, πr^2 is particle cross-sectional area, $Q_{\text{ext}}(m, r)$ is the extinction efficiency factor, m is the complex index of refraction, and $n(r)$ is the number of particles for a given radius. $Q_{\text{ext}}(m, r)$ is a function of both composition and size of a particle and describes the effects of both scattering and absorption due to the interaction of a particle with radiative energy of a specified wavelength. Changes in the size, composition or distribution of constituents or suspended particles in the atmosphere directly affect the amount of extinction observed. Therefore, measurement of extinction can inversely lead to knowledge of the characteristics of the atmosphere's particulate distribution.

Scattering of solar radiation dominates other radiative transfer factors in the visible and NIR. Due to the near uniformity of molecular constituents both spatially and temporally for a given region, Rayleigh (molecular) scattering can be adequately calculated (Durkee et al., 1991). Removal of Rayleigh scattered radiance effects from satellite retrieval methods allows for quantification of scattering effects by suspended aerosols only. The effect of scattering due to aerosols is approximated using Mie theory for spherical particles. For the cloud-free marine environment, the extinction coefficient is well represented by the scattering coefficient:

$$\sigma_{\text{scat}} = \int_0^{\infty} \pi r^2 Q_{\text{scat}}(m, r) n(r) dr \quad (2.2)$$

where $Q_{\text{scat}}(m, r)$ is the scattering efficiency factor, representing the ratio of total energy scattered in all directions to incident energy.

By integrating the extinction coefficient in the vertical through the atmosphere, optical depth is obtained:

$$\delta = \int_0^H \sigma_{\text{ext}} dz \approx \int_0^H \sigma_{\text{scat}} dz \quad (2.3)$$

Because satellite radiometers measure the radiative properties of the entire atmospheric column, quantification of total column optical depth is the objective of the satellite retrieval technique used in this study.

B. RADIATIVE TRANSFER SOLUTION

Equation 2.4 provides a general form for radiative transfer for a given solar wavelength in a plane parallel atmosphere is defined as (after Liou (1980)):

$$\begin{aligned} \mu \frac{dL_t(0; \mu, \phi)}{d\delta} = & L_t(\delta, \Omega) - \frac{\omega_o}{4\pi} \int_{4\pi} L_t(\delta, \Omega) p(\Omega, \Omega') d\Omega \\ & - \frac{\omega_o}{4\pi} \pi F_o p(\Omega - \Omega_o) e^{-\delta/\mu_o} \end{aligned} \quad (2.4)$$

where μ is the cosine of satellite zenith angle (θ), μ is the cosine of Sun zenith angle (θ_o), ϕ is the relative azimuth between the satellite and Sun, L_t is diffuse radiance ($\text{W/m}^2 \mu\text{m sr}$), Ω is the solid angle defined by θ and ϕ , ω_o is the single scattering albedo, p is the scattering phase function, and F_o is the incoming solar radiance at the

top of the atmosphere. The single scatter albedo (ω_o) is defined as the ratio of the scattering coefficient to the extinction coefficient. The terms on the right hand side of Equation 2.4 represent the total radiative energy in a beam, the energy scattered into the beam due to multiple scattering, and the energy scattered into the beam due to single scattering, respectively.

For atmospheres with small optical depths such as the cloudless, marine atmosphere, contribution to Equation 2.4 by multiple scattering is negligible. Solution to Equation 2.4 without multiple scattering is known as the single scattering approximation (after Liou (1980)):

$$L_t = \frac{\omega_o \mu_o F_o}{4(\mu + \mu_o)} p(\psi_s) \left[1 - e^{-\delta(\frac{1}{\mu_o} + \frac{1}{\mu})} \right] \quad (2.5)$$

where ψ_s is the scattering angle.

After accounting for ozone, Rayleigh and ocean surface effects, Durkee *et al.* (1991) show that in this environment δ_a is small enough to reduce Equation 2.5 to:

$$L_a = \frac{\omega_o F_o}{4\mu} p(\psi_s) \delta_a \quad (2.6)$$

where the subscript "a" denotes aerosol related quantities.

Solution of Equation 2.6 for aerosol optical depth (δ_a) requires knowledge of the measured radiance at the satellite radiometer (L_a) due to aerosol scattering at a given wavelength, the single scatter albedo, the incoming solar radiance (F_o), the satellite zenith angle (represented by μ), and the scattering phase function (P). Since typical marine aerosol are weak absorbers, the scattering and

extinction coefficients are approximately equal for this environment, and the single scatter albedo is approximately one. The satellite zenith angle is determined by the satellite-Earth geometry. The other terms are described in detail below.

1. Aerosol Radiance (L_a)

Equation 2.7 describes the aerosol scattered radiance measured by a satellite radiometer through a simple, linear expression (after Gordon and Clark, 1980):

$$L_a = L_t - L_r - (L_s + L_g)\tau \quad (2.7)$$

where L_r is radiance due to Rayleigh Scatter, L_s is surface reflected radiance, L_g is Sun glint radiance, and τ is transmittance of the atmosphere. For satellite radiometer window channels in solar wavelengths, τ can be approximated as one with less than 10% error.

To remove ozone absorption effects in the upper atmosphere, a correction to L_t is made by dividing L_t by the slant-path transmittance due to atmospheric ozone as in Equation 2.8:

$$L_t = \frac{L_t}{e^{-\delta_{o_3} \left(\frac{1}{\mu_o} + \frac{1}{\mu} \right)}} \quad (2.8)$$

where δ_{o_3} is ozone optical depth.

Radiance contribution associated with Rayleigh scatter is calculated using a two-stream model by Turner (1973):

$$L_r = \frac{E_o e^{-\delta_{o3}(\frac{1}{\mu_o} + \frac{1}{\mu})}}{4\pi(\mu_o + \frac{\delta_r}{2})} * \left[\left\{ \frac{1}{2} \delta_r [p^r(\psi_{s+}) + p^r(\psi_{s-})] + \left[p^r(\psi_{s-}) \mu_o + 2\mu_o^2 \frac{\bar{\rho}}{1 + (1 - \bar{\rho})\delta_r} \right] \left(1 - e^{-\delta_r/\mu} \right) \right\} + \left\{ \frac{1}{2} [p^r(\psi_{s+}) + p^r(\psi_{s-})] - \left[4\mu_o^2 \frac{\bar{\rho}}{1 + (1 - \bar{\rho})\delta_r} \right] \left((\delta_r + \mu) e^{-\delta_r/\mu} - \mu \right) \right\} \right] \quad (2.9)$$

where E_o is incoming solar irradiance, δ_r is Rayleigh optical depth, $p_r(\psi_s)$ is the Rayleigh scattering phase function (equal to $3/4(1+\cos^2(\psi_s))$ where $+$ indicates forward scattering and $-$ indicates back scattering, and ρ is reflectivity of seawater.

L_s is not modeled. Ramsey (1968), using Coastal Zone Color Scanner (CZCS), demonstrated that surface reflectivity is less than 0.005 for red-visible wavelengths and zero for wavelengths greater than $0.7 \mu m$, consistent with the approximation of the ocean as a blackbody. Surface reflectance due to foam on the sea surface and subsurface reflectance due to suspended plankton/chlorophyll are the major contributors to L_s . Koepke (1984) provides a measure of foam reflectance in the visible spectrum based on wind speed from surface leaving radiance measurements ranging from near-zero in winds below 5 m/s to 0.02 in winds in

excess of 20 m/s. Ignatov et al. (1995) report subsurface reflectance at $0.63 \mu\text{m}$ in the open ocean with chlorophyll concentrations less than 0.25 mg/m^3 on the order of 0.0014 ± 0.0006 . For this thesis, the combined effect of foam and subsurface reflectance is estimated at 0.002 at $0.63 \mu\text{m}$ and 0.005 at $0.86 \mu\text{m}$. Directional reflectance due to the variation in refractive index between the atmosphere and ocean is treated in the phase function term described below.

Contamination by specular glint (L_g) of the surface of the ocean for low Sun angles can be a problem for certain satellite-Earth-Sun geometries. Special care must be taken to review a satellite image for Sun glint signatures and avoid optical depth retrievals in contaminated regions. L_g is not modeled; in glint free areas L_g is assumed to be zero.

2. Scattering Phase Function (P)

The scattering phase function describes the probability of energy scattering into a specific direction. The scattering phase function is dependent on the radiation wavelength and size, composition, and distribution of atmospheric constituents. For Rayleigh scattering, the phase function is well understood; this approximation is used in the Turner solution above (Equation 2.9). For larger particles, Mie theory is used to quantify the scattering phase function with wavelength, size distribution and refractive index as inputs. To accurately quantify the phase function, one must have knowledge of the aerosol size distribution and composition. This creates an ill-posed problem since it is precisely the aerosol characteristics desired as a result of this retrieval method. To parameterize the phase function, several methods may be used. A common approach incorporates a phase function

empirically fit using measured averaged size distributions and characteristics for a region. Another uses the sensitivity of the phase function to radiative differences between two (or more) wavelengths to parameterize the phase function. Chapter IV contains a detailed description of both methods.

When solar radiation scatters due to molecular or aerosol interaction, the scatter can be described as both direct (directly towards the receiving sensor) or diffuse (scattering at other angles which may eventually scatter or reflect back to the sensor). Based on Sun-Earth-satellite geometry, both a forward ($0-90^\circ$) and back scattering angle ($90-180^\circ$) are defined. Treatment of the direct scatter is accomplished by using the value of the phase function in the linear single scattering model corresponding to the back scattering angle. Without true multiple scattering in the model, effects of diffuse scatter reflecting off the ocean surface (bi-directional reflection) can be estimated using Fresnel reflection coefficients and the forward scattering angle ($0-90^\circ$). An effective phase function is defined by Equation (2.10):

$$P_{\text{eff}} = P_- + P_+ [r_{\mu_0} + r_\mu] \quad (2.10)$$

where P_{eff} is the effective phase function, P_- is the value of the phase function at the back scattering angle, P_+ is the value of the phase function at the forward scattering angle, and r is the Fresnel reflection coefficients at both μ_0 and μ . Fresnel reflection coefficients are given in Equation (2.11):

$$r_{\theta} = 0.5 \left[\left(\frac{\sin(\theta_i - \theta_t)}{\sin(\theta_i + \theta_t)} \right)^2 + \left(\frac{\tan(\theta_i - \theta_t)}{\tan(\theta_i + \theta_t)} \right)^2 \right] \quad (2.11)$$

where θ_i is the angle of incidence and θ_t is the angle of transmission. From Snell's law, $\theta_t = \sin^{-1}(\sin(\theta_i)/m)$ where m is the index of refraction of seawater (1.33). The effective phase function describes an estimate of the increase in probability of solar radiation received at the sensor due to two possible paths: (1) direct transmission of solar energy to the sea surface, air-ocean interface reflectance, and forward scatter off an aerosol, or (2) forward scatter off an aerosol, air-ocean interface reflectance, and direct transmission to the sensor.

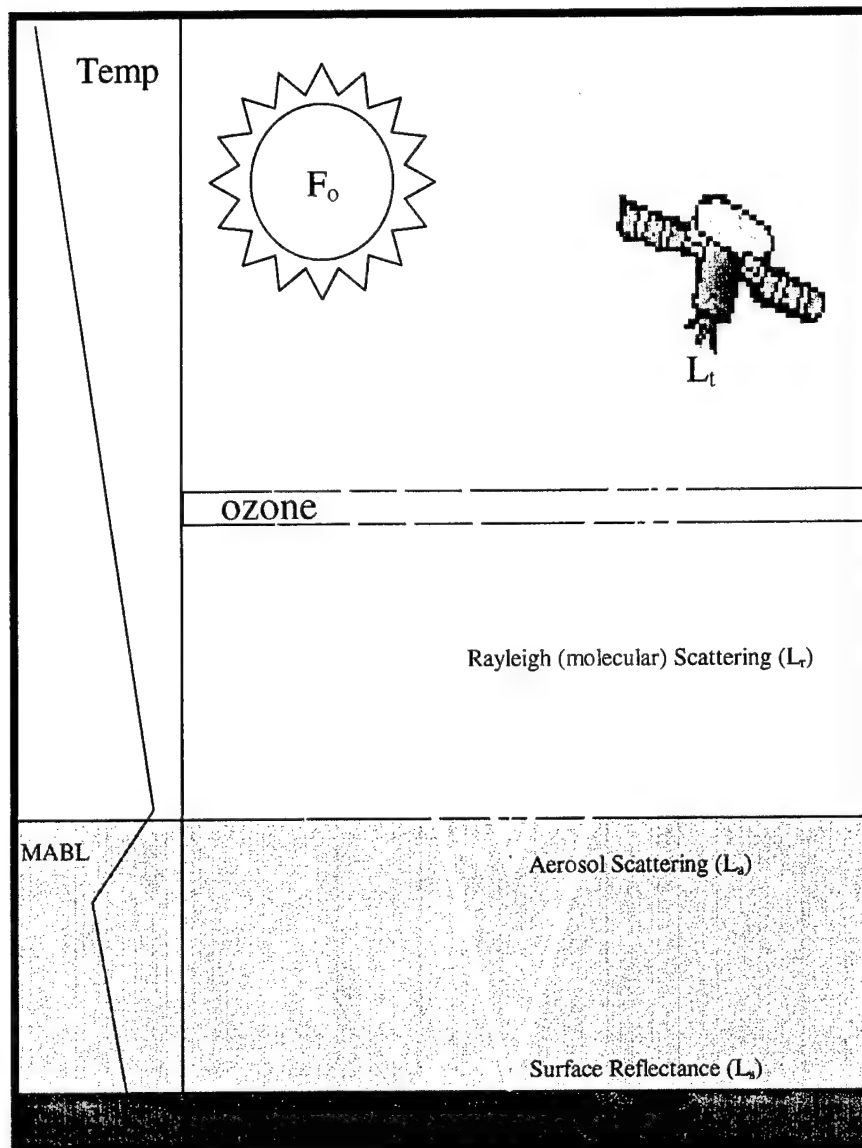


Figure 2.1. Radiative Transfer in the cloudless, marine environment. On the left, a typical atmospheric temperature profile depicting the marine atmospheric boundary layer (MABL) is included. Water vapor and aerosols are assumed to be confined to the MABL. Various scattering paths of incoming solar radiation (F_0) from Sun to satellite are shown in the right panel. Radiance variations along these paths measured by satellite radiometers (L_t) are primarily caused by upper atmosphere ozone absorption, Rayleigh (L_r) and aerosol (L_a) scattering, and ocean surface reflectance (L_s).

III. DATA

In order to validate the optical depth retrieval method described in this study, reference data sets were chosen based on the availability of *in situ* measurements of aerosol distributions and/or optical depth measurements. To the greatest extent possible, *in situ* measurements are matched to satellite observations both spatially and temporally. This chapter will briefly describe the data sets and instrumentation used to collect the data used in this study.

A. TARFOX DATA SETS

The TARFOX field experiment was designed as a closure study to better understand the radiative forcing effects of aerosols. TARFOX was conducted in the continentally-influenced environment off the eastern coast of the United States near Wallops Island, Virginia from 10-31 July 1996. During TARFOX, a variety of aerosol conditions ranging from relatively clean to moderately polluted were observed and measured. *In situ* measurements were conducted by airborne platforms including the University of Washington's (UW) C-131A and the United Kingdom's (UK) Meteorological Research Flight C-130 (see Russell et al., 1996). The UW C-131A was outfitted with NASA AMES Airborne Autotracking Sunphotometer for aerosol optical depth, a Passive Cavity Aerosol Spectrometer Probe (PCASP) for aerosol size distributions, and various meteorological observing instruments (temperature, dew point, pressure). The UK C-130 carried a PCASP, a Particle Soot/Absorption Photometer (PSAP) to measure aerosol absorption, and various meteorological observing instruments. Satellite imagery collected included full resolution NOAA 14 AVHRR (5 channel) and GOES 8 Imager (channel 1 and channel 4) data. The TARFOX Operations

Summary (Whiting et al., 1996) contains details of the field collection effort.

B. INSTRUMENTS

1. NOAA Advanced Very High Resolution Radiometer (AVHRR)

The AVHRR instrument is a component of the NOAA Polar Orbiting Operational Environmental Satellite (POES) series satellites. Current operational POES include the NOAA 12 and NOAA 14. These satellites are in Sun synchronous orbit (883 km) and provide two passes per day in the morning and evening, respectively. Due to current orbit design, NOAA 12 does not provide adequate daylight morning imagery for use in the aerosol optical depth retrieval in the mid latitudes and was not used in this study. The AVHRR instrument measures radiant and solar-reflected energy from sampled areas of the Earth in five spectral bands with a sub-satellite resolution of 1.1 km. Table 3.1 lists the characteristics of the individual radiometer channels for the AVHRR. (Kidwell, 1995)

Channel	Band Widths (μm)
1 (Visible)	0.58 - 0.68
2 (NIR)	0.725 - 1.10
3 (IR)	3.55 - 3.93
4 (IR)	10.3 - 11.3
5 (IR)	11.5- 12.5

Table 3.1. NOAA AVHRR Radiometric Channels

Channels 1 and 2 are used in the optical depth retrieval. Channels 4 and 5 are used in manual cloud screening analysis.

All AVHRR channels are calibrated prior to launch. Channels 1 and 2 of the AVHRR have no onboard calibration systems. Post calibration methods for these channels have been developed by the NOAA/NESDIS Office of Research Applications based on the results of Rao and Chen (1995). Calibration formulae are incorporated into the satellite image processing discussed in Chapter IV.

2. GOES Imager

This instrument is a major component of the NOAA Geosynchronous Operational Environmental Satellite (GOES) series satellites GOES 8 and GOES 9. Operating in a geosynchronous orbit at 36,000 km over equatorial sub-points at 75 W (GOES 8) and 135 W (GOES 9), this radiometer provides imagery from full-Earth disc images to small area scans due to a flexible scan system design. Like the AVHRR, the GOES Imager is a multiple channel radiometer which measures radiant and solar-reflected energy from the Earth. Unlike the AVHRR, spatial resolution is not the same for each channel. All GOES Imager channels are calibrated prior to launch. Similar to the AVHRR, the GOES Imager channel 1 does not have an onboard calibration system. No post-calibration methods for this channel have been developed or are planned for development. Table 3.2 lists the spectral and resolution characteristics of the GOES Imager. Channel 1 is used in the optical depth retrieval method described in this study. (*GOES-IJ/KLM SN03 Imager Data and Calibration Handbook*, 1994, and *GOES Calibration and Alignment Handbook for the Imager SN04 Instrument*, 1994)

Channel	Band Width (μm)	Resolution (km)
1 (Visible)	0.55 - 0.75	1
2 (IR)	3.80 - 4.00	4
3 (Water Vapor)	6.50 - 7.00	8
4 (IR)	10.20 - 11.20	4
5 (IR)	11.50 - 12.50	4

Table 3.2. GOES Imager Radiometric Channels

Only imagery from GOES 8 was used in this study due to the geographic location of TARFOX.

3. NASA AMES Airborne Autotracking Sunphotometer

By tracking the Sun, the NASA AMES Airborne Autotracking Sunphotometer measures the relative intensity of the direct incoming solar radiation in multiple spectral channels. This information is converted to optical depth. By flying an aircraft at low altitudes in cloud-free regions within the atmospheric boundary layer, total column optical depth can be well approximated. Table 3.3 lists the spectral bands for the six channels of the instrument. Instrument calibration is performed by NASA AMES prior to flight; the instrument is designed to maintain calibration within 1% during operation. Resolution of optical depth is on the order of 0.01. (Matsumoto et al., 1987)

Channel	Spectral Band (μm)
1	0.380
2	0.451
3	0.525
4	0.860
5	0.945
6	1.021

Table 3.3. NASA AMES Airborne
Autotracking Sunphotometer Spectral
Characteristics

During TARFOX only channels 1-3 and 6 were reported.

4. Passive Cavity Aerosol Spectrometer Probe (PCASP)

The PCASP is an airborne instrument designed to size aerosol distributions in the 0.1 μm to 3.0 μm range. The PCASP employs a He-Ne (632.8 nm) laser to sample aerosol size distribution from an aerodynamically focused jet which restricts the particle flow to a 150 μm diameter stream. A combination reflecting-refracting optical system collects light scattered from the laser beam by the aerosol in the jet and converts the resultant signal into particle size distribution. Distribution is segmented into 15 channels with a minimum size resolution of 0.02 μm in the smallest size channels, progressively weighted towards a maximum of 0.5 μm in the largest size channels. The instrument is calibrated prior to use using monodispersed spheres. (Passive Cavity Aerosol Spectrometer Probe (Airborne) PMS Model PCASP-100X 0.10 - 3.0 μm Operating Manual)

5. Particle Soot Absorption Photometer (PSAP)

The PSAP measures the aerosol absorption coefficient of an air sample based on the integrating plate technique. An external vacuum source provides an air sample to the PSAP; differences in the optical transmission of a filter due to aerosol deposition are converted to absorption using Beer's Law and a calibration transfer coefficient determined by the filter type. The PSAP is designed to give a continuous measurement of absorption coefficient with time averaged resolution of 5 to 300 seconds. The absorption coefficient is measured at 0.565 mm with a sensitivity of 10^{-6}m^{-1} for 1 minute averages. (*Particle Soot/Absorption Photometer (PSAP) Operation Procedures*)

IV. OPTICAL DEPTH RETREIVAL PROCEDURES

This chapter outlines the procedures used to calculate aerosol optical depths from the satellite imagery included in the reference data sets.

A. SATELLITE IMAGE RETREIVAL/DISPLAY

Satellite image retrieval and display was performed on the Terascan Earth Remote Sensing System by SeaSpace Corporation. Terascan allows display and enhancement of NOAA POES High Resolution Picture Transmission (HRPT) data and GOES variable (GVAR) formatted data at full resolution. Embedded routines in the Terascan system convert sensor radiance counts into albedo/brightness temperature, calculate required angles from Sun-Earth-satellite geometry, and map imagery from different sources to the same spatial grid for comparison. Imagery used in this study was previewed in Terascan prior to optical depth retrieval to conduct cloud and Sun glint screening. Terascan also offers a full suite of post processing enhancements which greatly aided the optical depth analysis.

B. OPTICAL DEPTH RETRIEVAL

The optical depth retrieval technique used for the GOES Imager and NOAA AVHRR data is an automated process which required the use of both Terascan and FORTRAN 77 code. The processing sequence is illustrated Figure 4.1.

Pre-processing consists of the use of Terascan commands to retrieve raw satellite images from the pass disk of the Terascan receiver system. Manual cloud and Sun glint screening is performed in this step.

The main processing of the data was completed using a mixture of Unix Borne scripts (with embedded Terascan

commands) and compiled FORTRAN code. The Unix scripts registered the raw files to a predetermined geographic area, calibrated the data (if required), calculated significant angles (satellite zenith, Sun zenith, relative azimuth, and scattering angle), and created an export binary file for mathematical processing in FORTRAN. The FORTRAN code calculated all radiative transfer calculations including optical depth. After calculation, the radiative transfer output from the FORTRAN code was imported back into Terascan format and assembled with the initial channel data.

Post-processing included the use of Terascan display and enhancement features to analyze the imagery.

C. RADIATIVE TRANSFER CODE

The FORTRAN code used to calculate optical depth from measured satellite radiance follows the theory of Chapter II and calculates a solution to Equation 4.10. The central value of the satellite channel's spectral response is used as the input wavelength. Calculation of the specific input variables into Equation 2.6 are described in this section.

1. Solar Irradiance/Solar Radiance

Input values for solar irradiance are determined by calculating a weighted average of solar irradiance integrated across the satellite radiometer channel spectral response. For the NOAA 12 and 14, values were taken from the *NOAA Polar Orbiter Data Users Guide* (Kidwell, 1995). For the GOES, spectral response functions for the GOES 8 and GOES 9 documented in the *GOES-IJ/KLM SN03 Imager Data and Calibration Handbook* (1994) and *GOES Calibration and Alignment Handbook for the Imager SN04 Instrument* (1994) were used to calculate the weighted solar irradiance. Table 4.1 lists the values of solar irradiance used for the various satellites/channels. Solar radiance is calculated

by dividing solar irradiance by π (E_o/π). Prior to input into the model, E_o is corrected for variation in the Earth-Sun distance.

Satellite	Radiometer Channel	E_o ($W/m^2 \mu m$)
NOAA 12	AVHRR Ch 1	1614
NOAA 12	AVHRR Ch 2	1050
NOAA 14	AVHRR Ch 1	1628
NOAA 14	AVHRR Ch 2	1030
GOES 8	Imager Ch 1	1629
GOES 9	Imager Ch 1	1617

Table 4.1. Values of Solar Irradiance

2. Ozone and Rayleigh Optical Depths

Input values for ozone and Rayleigh optical depths are determined by calculating a weighted average of reported ozone and Rayleigh optical depths by Elterman (1970) integrated across the satellite radiometer channel spectral response. Table 4.2 lists the values of both ozone and Rayleigh optical depths used for the various satellites/channels.

Satellite	Radiometer Channel	Ozone δ	Rayleigh δ
NOAA 12/14	AVHRR Ch 1	0.027	0.057
NOAA 12/14	AVHRR Ch 2	0.0021	0.019
GOES 8/9	Imager Ch 1	0.024	0.061

Table 4.2. Values of Ozone and Rayleigh Optical Depths

3. Scattering Phase Function

Parameterization of the scattering phase function is the most difficult part of the optical retrieval. Knowledge of aerosol size distribution is required to accurately calculate the phase function from Mie theory. Since this

distribution is not known exactly without *in situ* aerosol measurement, the scattering phase function must be parameterized by other methods. For this study, two methods are used. One method uses an empirically derived aerosol size distribution to calculate the scattering phase function. The second method uses multispectral radiance differences measured by a satellite to parameterize the scattering phase function. These methods are described below.

a. NOAA/NESDIS derived Scattering Phase Function

An empirically derived aerosol size distribution provided by the NOAA/NESDIS Satellite Research Laboratory is used to calculate the scattering phase function. The aerosol size distribution is a single-mode log-normal distribution with a mode radius of 0.1 μm , standard deviation (σ) of 2.03, and a complex refractive index $m = 1.4+0.0i$ (Ignatov et al, 1995). This type of scattering phase function is applied statically across the entire image during retrieval and does not account for variations in the aerosol size distributions known to exist, especially in coastal regions. Figure 4.2 and 4.3 illustrate the aerosol size distribution and phase functions at 0.63 μm and 0.86 μm .

b. Particle Size Parameter (S_{12}) Derived Scattering Phase Functions

Durkee et al. (1991) proposed a method of parameterizing the scattering phase function based on a ratio of the aerosol radiance measured in the channels 1 (visible) and 2 (NIR) of the NOAA AVHRR. Because scattering efficiency (Q_{scat}) of an aerosol distribution is wavelength dependent, scattering for a specific aerosol population

peaks when the radius of the aerosol is nearly equal to the radiation wavelength. Subsequently, radiance counts measured by the AVHRR visible and NIR channels will change with aerosol size distribution changes such that the ratio of channel radiances will be larger for smaller size particle distributions and smaller for larger size particle distributions.

Durkee et al. (1991) termed the ratio of the channel aerosol radiances the particle size parameter, S_{12} . Since S_{12} varies pixel-by-pixel across the entire satellite image, the scattering phase functions can be parameterized pixel-by-pixel, allowing variations in aerosol distributions to be properly factored into the optical depth retrieval.

For the optical depth retrieval, the scattering phase functions and extinctions for seven model aerosol size distributions (M0-M6) are calculated using Mie theory. These distributions consist of one single-mode and six two-mode log-normal distributions with varying mode radii and standard deviations designed to model the typical variations of aerosol distributions in the marine atmosphere. The first mode models the background aerosol while the second mode models ocean-produced aerosol. The NOAA/NESDIS aerosol size distribution represents a rough approximation to the average of these distributions. The refractive index used is the same as the NOAA/NESDIS model. Table 4.3 lists the mode radii and standard deviations used. Figures 4.4, 4.5, and 4.6 illustrate the resulting aerosol size distributions and the corresponding scattering phase functions at 0.63 μm and 0.86 μm .

Model	Mode Radii (μm)	Std Dev (σ)
M0	0.1/0.0	1.7/0.0
M1	0.1/0.3	1.7/2.1
M2	0.1/0.3	1.7/2.2
M3	0.1/0.3	1.7/2.35
M4	0.1/0.3	1.7/2.51
M5	0.1/0.3	1.7/2.6
M6	0.1/0.3	1.7/2.7

Table 4.3. Mode Radii and Standard Deviations for Model Aerosol Size Distributions

The calculated scattering phase functions and extinction coefficients for these distributions are converted to S_{12} using the following equation (based on linear single scattering theory):

$$S_{12} = \frac{L_{ch1}}{L_{ch2}} \approx \frac{P_{ch1} F_{och1} \sigma_{extch1}}{P_{ch2} F_{och2} \sigma_{extch2}} \quad (4.1)$$

Due to water vapor absorption in channel 2 of the AVHRR, a correction to S_{12} is made following Mahony (1991) based on the split-channel (channels 4 and 5) water vapor retrieval proposed by Dalu (1986). The resulting S_{12} values for each aerosol model are shown in Figure 4.7.

During processing of the satellite radiance data in the optical depth retrieval code, S_{12} values are calculated for each pixel from AVHRR channel 1 and channel 2 data. Computed S_{12} values along with scattering angle are then entered into a lookup table representing Figure 4.7 to determine the model aerosol distribution (Figure 4.4) best represented by the observed radiance measurements. Using

the scattering angle and model size distribution, phase function values are then selected from lookup tables based on Figures 4.5 and 4.6.

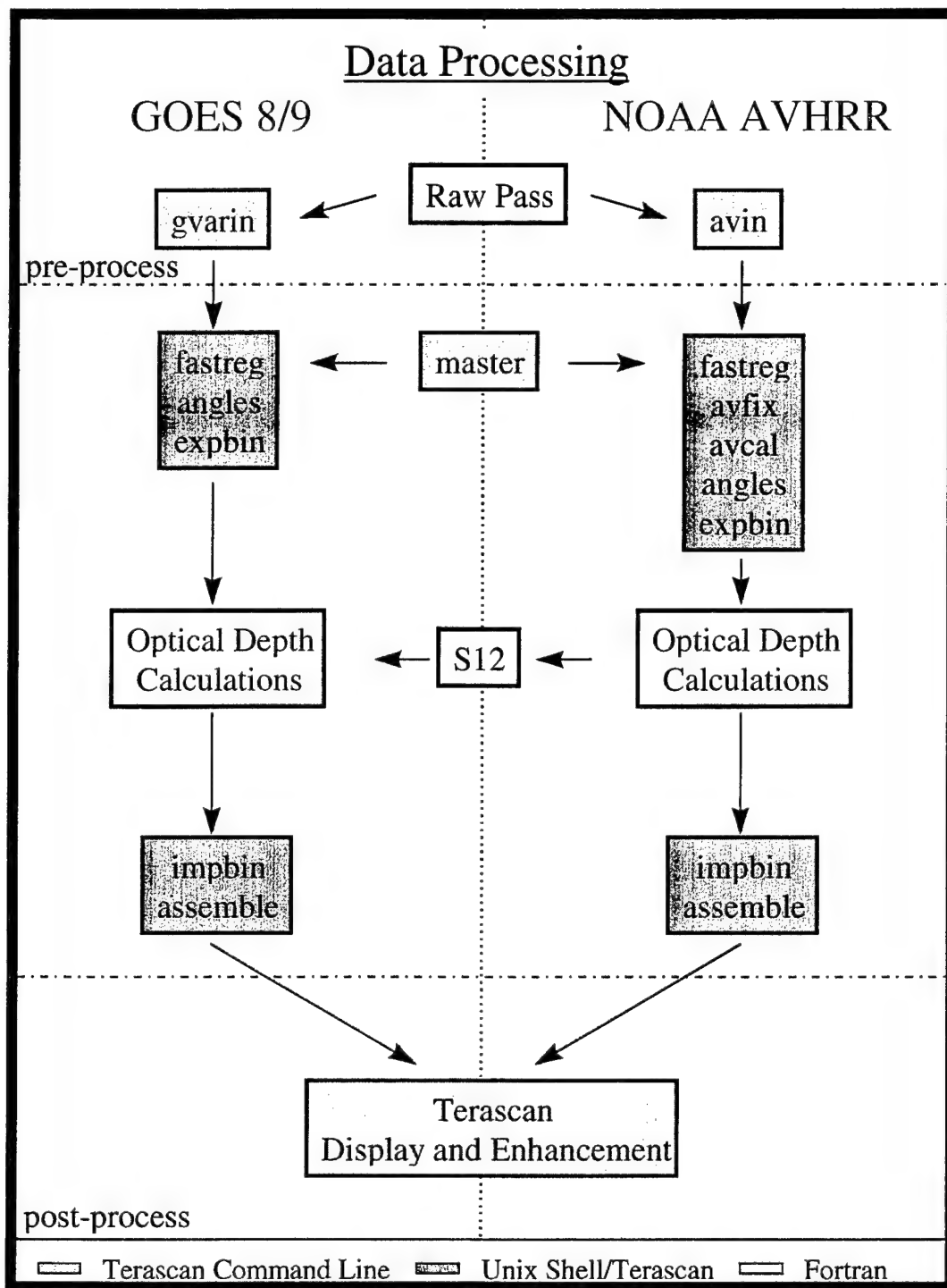


Figure 4.1. Satellite Aerosol Optical Depth Retrieval.

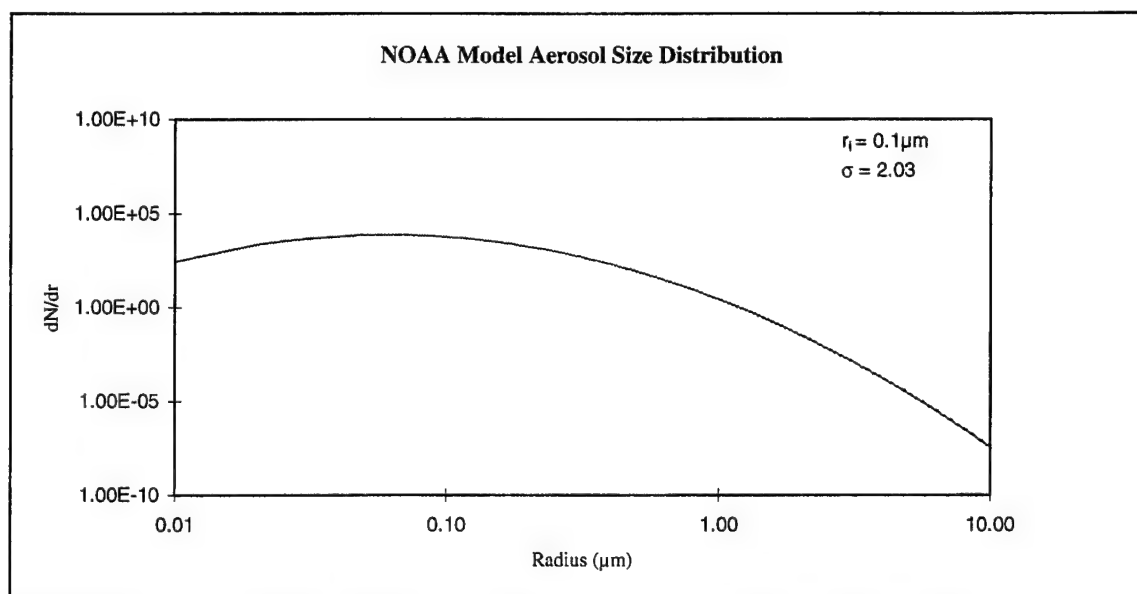


Figure 4.2. NOAA/NESDIS Aerosol Size Distribution.

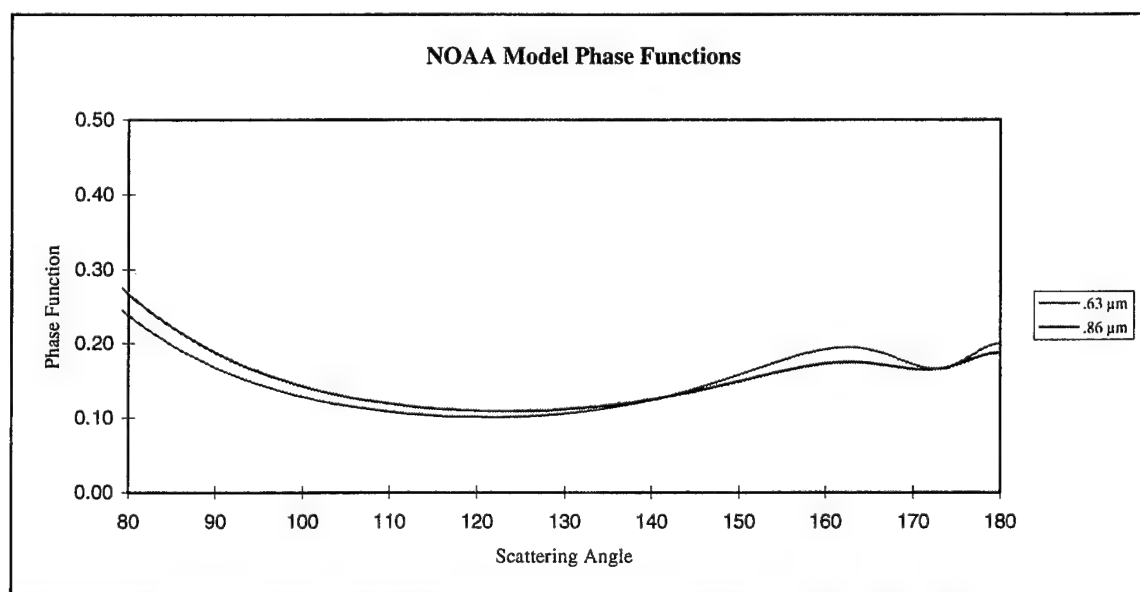


Figure 4.3. NOAA/NESDIS Scattering Phase Functions.

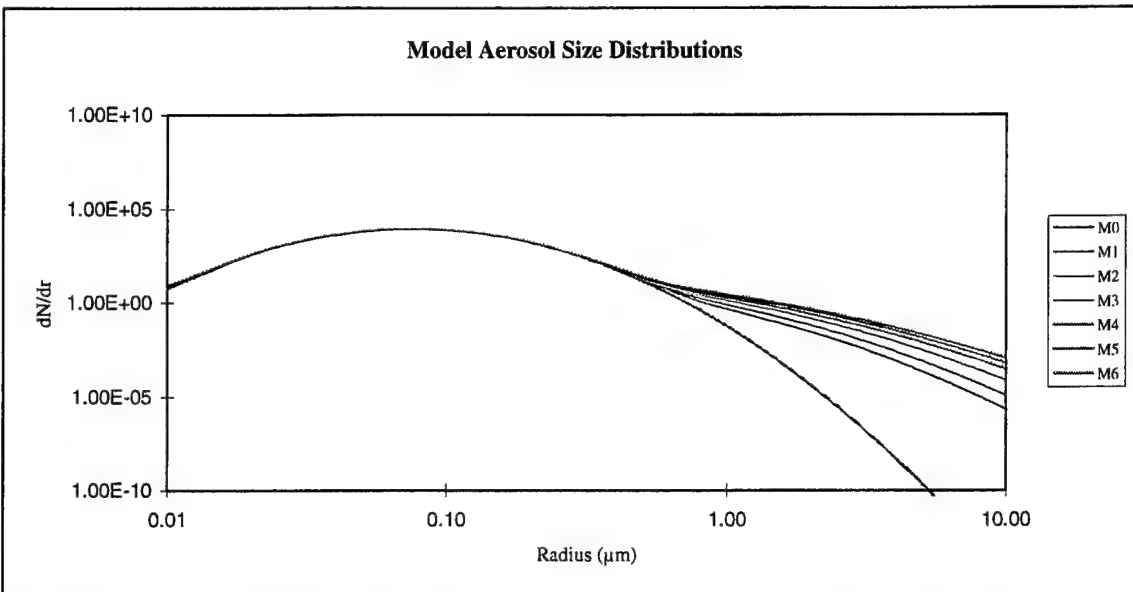


Figure 4.4. Model Aerosol Size Distributions. M0-M6 correspond to model two-mode, lognormal aerosol distributions with M0 representing the background (continental) aerosol mode and M6 representing the largest oceanic aerosol mode.

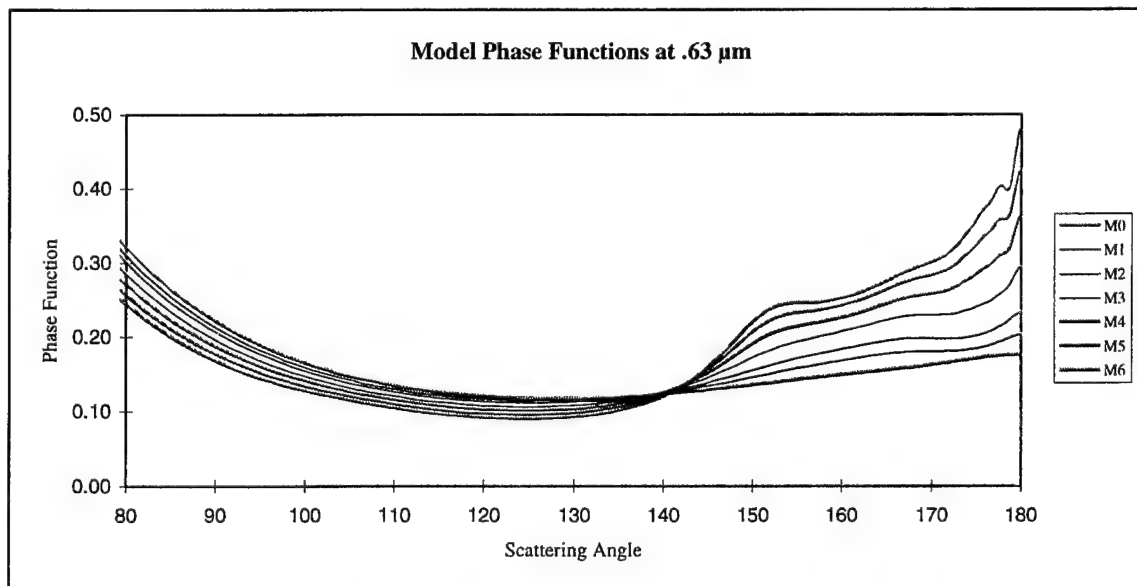


Figure 4.5. Model Phase Functions at 0.63 μm . M0-M6 correspond to model two-mode, lognormal aerosol distributions with M0 representing the background (continental) aerosol mode and M6 representing the largest oceanic aerosol mode.

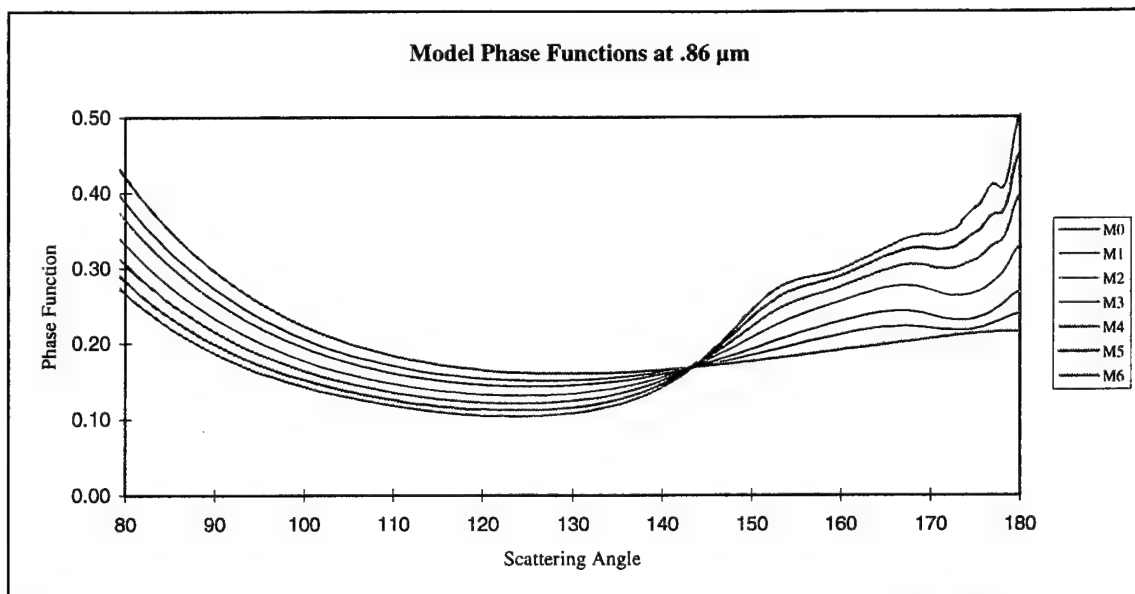


Figure 4.6. Model Phase Functions at 0.86 μm . M0-M6 correspond to model two-mode, lognormal aerosol distributions with M0 representing the background (continental) aerosol mode and M6 representing the largest oceanic aerosol mode.

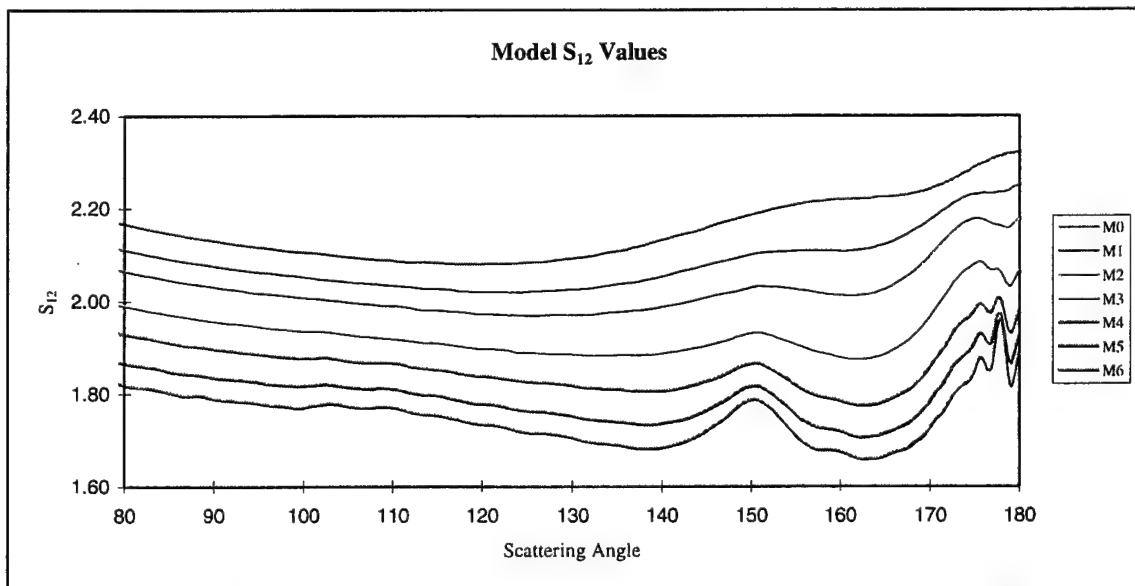


Figure 4.7. Model S_{12} Values. M0-M6 correspond to model two-mode, lognormal aerosol distributions with M0 representing the background (continental) aerosol mode and M6 representing the largest oceanic aerosol mode. S_{12} values are calculated using linearized, single-scattering theory.

V. RESULTS

A. OVERVIEW OF TARFOX

During the TARFOX period, 10-31 July 1996, coordinated aircraft measurements and satellite overpasses were limited due to a number of factors. The weather played a major role due to a series of low pressure systems and associated cloudiness repeating approximately every 2-3 days over the TARFOX area. Another limitation was the viewing geometry of the NOAA 14, eliminating 6 NOAA 14 overpasses from the data set due to Sun glint contamination (10, 17, 20, 27, 28, 29 July). Based on all factors, the data set selected for this thesis included aircraft, NOAA 14, and GOES 8 data on 16, 23, and 25 July. Of these days, only 25 July had a complete set of spatially and temporally coordinated sunphotometer, PCASP, PSAP and satellite data (partially due to data access limitations imposed by some of the TARFOX participants). Additionally, it was the most cloud-free day analyzed (see Figure 5.1). Subsequently, the majority of the results of this study are concentrated on data from 25 July. An additional day of coordinated sunphotometer data from a land site on Bermuda and NOAA 14 overpass on 18 July are also analyzed; unfortunately, GOES 8 imagery extending over Bermuda was not archived during this period due to storage limitations. Some UK C-130 PCASP data taken on days without useful NOAA 14 imagery are also presented to illustrate variability of aerosol loading in the TARFOX area. Table 5.1 lists the aircraft flights, satellite overpasses and data used.

Date	Time	Aircraft/Satellite	Data
16 July 96	1840 UTC	NOAA 14	AOD
16 July 96	1853 UTC	UW C-131A (Flight 1727)	sunphotometer
18 July 96	1816 UTC	NOAA 14	AOD
18 July 96	1656- 1956 UTC	Bermuda	sunphotometer
21 July 96	1414 UTC	UK C-130 (Flight A466)	PCASP PSAP
23 July 96	1906 UTC	NOAA 14	AOD
23 July 96	1839 UTC	UW C-131A (Flight 1732)	sunphotometer
25 July 96	1432 UTC	GOES 8	AOD
25 July 96	1435 UTC	UW C-131A (Flight 1734)	PCASP
25 July 96	1842 UTC 1906 UTC	UW C-131A (Flight 1735)	sunphotometer PCASP
25 July 96	1842 UTC	NOAA 14	AOD
25 July 96	1845 UTC	GOES 8	AOD
25 July 96	2050 UTC	UK C-130 (Flight A469)	PCASP PSAP
25 July 96	2045 UTC	GOES 8	AOD
27 July 96	2203 UTC	UK C-130 (Flight A470)	PCASP PSAP

Table 5.1. TARFOX Data and Sensors Used in Study.

B. 25 JULY 1996

1. Weather

Pre-frontal conditions existed over the TARFOX area on 25 July 1996 with southeasterly flow at 5-10 kts due to a 1015 mb low pressure center forming inland over the North Carolina/Virginia border. Figure 5.1 provides a NOAA 14

AVHRR channel 1 visible image of the experiment area. A broad area of low clouds associated with an easterly moving low pressure center is present in the northeast corner of Figure 5.1. Some cumuloform cloudiness associated this low center's dissipating trailing cold front exists in the southern region of the image. Otherwise, generally clear conditions were present in the flight areas near 38N 74.5W. With the southeasterly flow, an oceanic aerosol distribution is expected off the coast of the U.S..

2. Absorption

In order to test the assumption that absorption due to aerosols in the cloud-free marine environment is much smaller than scattering and, therefore, negligible, PSAP data measured by the UK C-130 was analyzed. Figure 5.2 provides the PSAP measured absorption coefficient for flight A469 on 25 July 1996. Additionally, PSAP absorption coefficients for flights A466 and A470 are included for reference. Comparison of Mie calculated scattering coefficients based on PCASP aerosol size distributions for the same flight profiles suggest that absorption is at least an order of magnitude smaller than scattering. Resulting estimates show that $\omega_0 \approx 0.97-0.99$. Therefore, assuming zero absorption results errors in ω_0 of less than 5%. At $0.63 \mu\text{m}$, $\omega_0 = 0.98$ corresponds to a complex index of refraction of $1.4 + 0.002i$. Using this value in phase function calculations based on PCASP size distributions from flight A469 indicate that assuming zero absorption also leads to less than 5% error in the MIE calculated phase function (see Figure 5.3).

3. Water Vapor

In order to validate water vapor corrections in channel 2 of the AVHRR, estimates of column water vapor were made using temperature and dew point measurements during flight 1735. Figure 5.4 provides the calculated water vapor profile measured during an ascent of flight 1735. In order to estimate total column water vapor, it was assumed that water vapor above the maximum height of the profile was zero and a 4th order polynomial fit to the profile was integrated across the depth of the profile. This resulted in a value of 1.77 gm/cm². Using the Dalu (1986) split-channel (AVHRR channel 4 - channel 5) technique in a 10x10 pixel box over the ascent region of flight 1735, total column water vapor was retrieved from the 1842 UTC NOAA 14 overpass. Resulting values of retrieved total column water vapor from the AVHRR were 2.59 gm/cm² with a standard deviation of 0.14. Both values lie within the climatological extremes of atmospheric water vapor; uncertainty in the amount of water vapor above the measured profile possibly accounts for the differences in values. Comparison of the effects of these differences on S_{12} and retrieved phase function indicate that a 30% difference in water vapor results in an approximate difference of 1-2% in S_{12} and less than 3% in phase function.

4. Aerosol Distributions/Phase Functions

a. 25 July Intercomparisons

Comparison of PSCAP data collected during ascent/decent of flights 1734, 1735, and 1736 to model aerosol size distribution provided some interesting results. Note that absolute calibration between the PCASP instruments used on the two aircraft had not been accomplished at the time of this study; therefore, some differences between

measured aerosol distributions may be due to the use of two instruments. Figures 5.5 and 5.6 contain measured and model aerosol size distributions in terms of number concentration (dN/dr) and volume ($dV/d\log r$). Good correlation between the aircraft measured distributions is illustrated, suggesting a nearly homogeneous air mass present over the TAFROX area both spatially and temporally. Based on the measured S_{12} values from the 1842 UTC NOAA 14 overpass, phase functions based on aerosol models M2 and M3 were selected by the satellite retrieval algorithm and are included for comparison.

Significant departures in both dN/dr and $dV/d\log r$ between measured and model distributions in the 0.1 to 0.7 μm radius range are noted. At radii larger than 0.7 μm , models M2 and M3 fit the measured data well in dN/dr . Distribution differences are more apparent in the $dV/d\log r$ plots; however, the two-mode M2 and M3 models demonstrate some skill at modeling the mode radii of the measured distributions but not the amplitude (up to 95% error). A third, smaller mode near 0.8 μm is not modeled in M2 or M3. The NOAA/NESDIS single-mode model is the worst fit to the measured distributions; however, this distribution broadly captures the mode near 0.8 μm in both dN/dr and $dV/d\log r$.

Figures 5.7 and 5.8 profile the potential temperature and relative humidity (RH) observed along the ascent/descent tracks of flights 1735 and A469. Note the consistency in the lower tropospheric structure. The shallow mixed layer (250m) and relatively high RH (50-60%) between 250 m and 3500 m is indicative of a maritime air mass. This is consistent with the wind field observed on 25 July 1996. The characteristically high number and low volume of particles $< 0.7 \mu m$ observed may be due to the longevity of the aerosol suspended over the ocean.

Figures 5.9 and 5.10 show the calculated phase functions from both measured and modeled size distributions at 0.63 μm and 0.86 μm , respectively. With the exception of the NOAA/NESDIS phase function at 0.86 μm , all modeled phase functions are 20-40% larger than the PCASP derived phase functions in the 160-180° back scattering angles (scattering angle for 1842 UTC NOAA 14 overpass 168°). Despite errors in magnitude, M2 and M3 fit the shape and slope of the derived phase functions. Characteristic sinusoidal patterns in the NOAA/NESDIS phase function are not present in the measured distribution phase functions. Also, in comparison of PCASP derived phase functions at 0.63 μm and 0.86 μm , an increase in phase function across all scattering angles is observed between the two wavelengths. This characteristic is not observed in the NOAA/NESDIS phase function, but is well represented in the M1-M6 phase functions.

Based on these observed differences in measured and modeled phase functions on 25 July 1996, errors in satellite retrieved aerosol optical depth should be on the same order due to the linearity of the algorithm (Equation 2.6).

b. 21, 25, and 27 July Intercomparisons

To understand the variability of the aerosol distributions during TARFOX, variations in UK C-130 PCASP measured aerosol size distributions, atmospheric boundary layer profiles, and calculated phase functions collected during flights A466, A469, and A470 are analyzed. Figures 5.11 and 5.12 provide comparisons of observed and modeled distributions in number concentration and volume, respectively. Figures 5.13 and 5.14, the corresponding boundary layer profiles, show a definite change in air mass occurs between 21 July and 25 July and again from 25 July to

27 July. The depth of the mixed layer (~ 1500 m) and the low relative humidities above this level on 21 and 27 July suggest an air mass of continental origin. This is consistent with northwesterly flow observed over the TARFOX area on 21 and 27 July. With the change in air mass, large variations in both aerosol number concentration and volume are present, especially in the smallest mode. Variability in the aerosol distribution is expected; however, modeled variability does not adequately capture the observed aerosol fluctuations. Because of lower aerosol number concentration and volume on 21 and 27 July, model estimates between M0 and M3 are expected over the entire period.

From Figures 5.15 and 5.16, error in the model size distributions lead to approximately 20-40% error in the model phase function based on expected S_{12} . These results are consistent with the results of the intercomparison of data on 25 July.

5. NOAA 14 Aerosol Optical Depth Retrieval

Sunphotometer aerosol optical depth data collected onboard flight 1735 during low-level portion of the flight was used in the validation of NOAA 14 retrieved aerosol optical depth from the 1842 UTC overpass. Figure 5.17 demonstrates good agreement between sunphotometer measured extinction and extinction calculated from measured size distributions from flights 1734, 1735 and A469, especially at NOAA 14 channel 1 and 2 wavelengths. The sunphotometer data represented in Figure 5.17 reflects an average of the low level portion of flight 1735 with error of $\pm 6\%$ based on standard deviation of the measurements. Figure 5.18 presents sunphotometer aerosol optical depths collected during flight 1735. Only data at $0.38 \mu\text{m}$, $0.451 \mu\text{m}$, $0.525 \mu\text{m}$ and $1.021 \mu\text{m}$ were recorded during the flight. Values at

0.63 μm and 0.86 μm were derived from a power law fit to the reported data.

Figure 5.19 represents the 1842 UTC NOAA 14 retrieved aerosol optical depth; the low level portion of flight 1735 is represented by the red track. Figures 5.20 and 5.21 represent comparisons of satellite retrieved aerosol optical depth collected in a box surrounding the flight 1735 flight track and sunphotometer data at 0.63 μm and 0.86 μm , respectively. Despite large errors in the phase function reported above, the satellite data fits closely to the sunphotometer observed data in magnitude and shape. This result suggests that the retrieval technique is sensitive to observed aerosol variation within the sample region.

A multiple-scattering radiative transfer model with bi-directional surface reflectance was used to investigate this unexpected fit. The model, the Second Simulation of Satellite Signal in the Solar Spectrum (Six S) model (Vermote et al. 1995), includes surface reflectance due to direct and diffuse radiance. After conducting simulations using observed PCASP aerosol distributions from flight 1735, observed Sun-Earth-satellite geometries along the flight 1735 track, and observed wind speed/direction, analysis of sunphotometer, Six S, and NOAA 14 AVHRR aerosol optical depths were completed. The calculated Six S model aerosol optical depth at 0.63 μm fit the sunphotometer observed data to 0.01 optical depth accuracy. Comparison of Six S calculated aerosol radiance (8.815 $\text{W/m}^2 \text{ sr } \mu\text{m}$) to NOAA 14 derived aerosol radiance (9.11 $\text{W/m}^2 \text{ sr } \mu\text{m}$) showed close agreement; this suggests that linear treatment of Rayleigh scatter and foam and subsurface reflectance in the linear single scatter model is comparable to the non-linear Six S model. Figure 5.22 graphically illustrates the overall results of the comparison of the models. Four possible

solutions to the problem are represented using observed aerosol distributions: (1) Six S with a full bi-directional surface reflectance model, (2) Six S without a bi-directional surface reflectance model (multiple scattering solution), (3) linear single scattering solution without a bi-directional surface reflectance model, and (4) the linear single scattering solution with the bi-directional surface reflectance approximation used in this study. In a linear sense, the slope of these lines is representative of the effective phase function, where $L_a = p_{eff}(\psi_s)\delta_a$. Error between the multiple scattering solution without a specular surface and the linear single scattering solution without a specular surface is approximately 17% for aerosol optical depths observed. Error between the full Six S solution and the linear single scattering solution used in this study is approximately 22%. Since the Six S solution is non-linear, it is not possible to separate the contribution to satellite observed radiance due to multiple scattering from that due to spectral surface reflectance. Therefore, the total error in the satellite retrieved aerosol optical depths using the study algorithm is due in part to both lack of multiple scattering and approximating spectral surface reflection. By chance, the error in the phase function representation in the model is offset by these errors, resulting in the fit of retrieved aerosol optical depth to the sunphotometer data.

6. GOES 8 Aerosol Optical Depth Retrievals

Despite the compensating errors in the satellite aerosol optical depth retrieval algorithm, the algorithm was extended to the 1845 UTC GOES overpass. Figure 5.23 provides the retrieved GOES 8 aerosol optical depths using the 1842 UTC NOAA 14 S_{12} phase function parameterization. Figure 5.24 demonstrates the fit of the GOES data to the sunphotometer data, again in good agreement.

Based on the consistency of the aerosol distributions taken during flights 1734, 1735, and A469, S_{12} data from the 1842 UTC NOAA 14 overpass were applied to GOES 8 imagery at 1432 UTC and 2045 UTC. Figures 5.25 and 5.26 provide histograms of calculated aerosol optical depth and phase functions for these passes as well as the 1842 UTC NOAA 14 and 1845 UTC GOES 8 overpasses for an area of the imagery which remained cloud-free over the time span of the passes.

The similarity of the GOES 8 and NOAA 14 aerosol optical depth data in Figure 5.25 demonstrates the potential of the GOES Imager data in aerosol optical depth retrieval. Throughout the time period from 1432 to 2045 on 25 July 1996, the GOES 8 Imager scattering angle varied from 120° to 145° while the NOAA 14 AVHRR scattering angle was 168° . Despite the variation in scattering angle and subsequent variation in phase function, consistency in retrieved aerosol optical depths between the two instruments was observed (Figure 5.25). Although the error in magnitude of the model phase function was on the order of 20-40%, the overall shape and slope of modeled phase functions had to be well represented in the algorithm in order to account for the close fit of the retrieved aerosol optical depths. Due to the linearity of the solution, any significant deviation in the shape and/or slope of the model aerosol distribution to the observed aerosol distribution would have resulted in significant variation in retrieved optical depths at each scattering angle. In the homogeneous offshore environment on 25 July, application of S_{12} forward and backward in time appears reasonable.

It is expected that degradation of the S_{12} information with time will occur and S_{12} application to GOES data will be limited temporally. These limitations require further

study with a larger data set in varied aerosol loading conditions.

Comparison of Figures 5.20 and 5.24 also illustrate the aerosol optical depth resolution expected from the two instruments based on digital resolution; the banding in the satellite data is due to the digitization steps of the satellite sensor. Aerosol optical depth resolution of the NOAA 14 AVHRR appears to be on the order of 0.04, while GOES 8 resolution is on the order of 0.8.

C. 18 JULY 1996

1. Weather

The focus area for data on 18 July 1996 was near Bermuda. The synoptic pattern over the island was characterized by a 1026 mb high resulting in generally clear skies with small clusters of low level cumulus. Winds 5-10 kts from the southwest were observed over Bermuda. Due to the trajectory of the air mass from the southwest, aerosol loading over Bermuda was relatively low due to lack of continental influence.

2. NOAA 14 Aerosol Optical Depth Retrieval

This case was selected for analysis based on low optical depths observed in the land based sunphotometer data over Bermuda. Figure 5.27 provides the histogram comparison of sunphotometer aerosol optical depth data (at .699 μm) taken between 1659 and 1959 UTC 18 July 1996 on Bermuda to aerosol optical depth retrieved from 1816 UTC NOAA 14 channel 1 in a cloud-free area just to the southwest of Bermuda. Note the good agreement in the data. The algorithm, despite noted errors, correctly computed lower aerosol optical depths. Also, this example shows the expected resolution of the NOAA 14 retrieved aerosol optical

depths. Due to the digitization steps of channels 1 and 2 of the AVHRR in this low optical depth case, channel 1 reflectance values varied by 5% while channel 2 reflectance values remained constant (near the low end of channel 2 sensitivity). This created variations in S_{12} of approximately 20% and corresponding phase functions variations of approximately 25%. The end result is aerosol optical depth resolution on the order of 0.04.

D. 16 JULY 1996

1. Weather

Mostly cloudy conditions associated with an easterly moving cold front existed to the east of the TARFOX operating area with some clearing off the east coast of Virginia behind the front. High cirrus was present over the area.

2. NOAA 14 Aerosol Optical Depth Retrieval

This case is presented to illustrate the importance of cloud screening. In an operational satellite aerosol optical depth retrieval algorithm, careful cloud screening must be accomplished. Figure 5.28 shows the aerosol optical depths retrieved from the 1840 UTC NOAA 14 overpass on 16 July 1996. Note the areas of obvious clouds with optical depths greater than 1. Near the flight path indicated for flight 1724, optical depth values retrieved were on the order of typical values observed during TARFOX. Review of corresponding enhanced NOAA 14 channel 4 infrared data (Figure 5.29) shows the presence of thin cirrus directly over the flight track at the satellite overpass time. Figure 5.30 provides the comparison of satellite derived and sunphotometer measured aerosol optical depths at 0.63 μm for this case. Despite errors in the retrieval

algorithm, close fit to observed data was observed in most cases; here an error in magnitude due to thin cirrus of approximately 80% is observed.

E. 23 JULY 1996

1. Weather

A 1009 mb low pressure system moving easterly over TARFOX area created overcast conditions over entire area. A small area of clearing to the southwest of Wallops Island was selected to conduct aircraft operations.

2. NOAA 14 Aerosol Optical Depth Retrieval

This case is presented to illustrate problems associated with aerosol optical depth retrievals in the boundaries of clouds. Figure 5.31 provides the 1906 UTC NOAA 14 aerosol optical depth retrieval for 23 July 1996. Notice that the entire area is cloud covered except for a small area of clearing to the southeast of Wallops Island directly off the coast in the vicinity of flight 1732 track. Corresponding NOAA 14 channel 4 data indicated no presence of upper level cirrus above flight 1732 track. Figure 15.32 shows the comparison of NOAA 14 retrieved and sunphotometer measured aerosol optical depth for this case at $0.63 \mu\text{m}$. Both measurements show considerable variability in this region. This is a good illustration of retrieval problems associated with the boundaries of clouds where significant moisture gradients occur. Certainly, the satellite retrievals will have difficulty in this environment, and in an operational setting, careful screening and elimination of retrieved measurements within the boundaries of clouds must be accomplished.

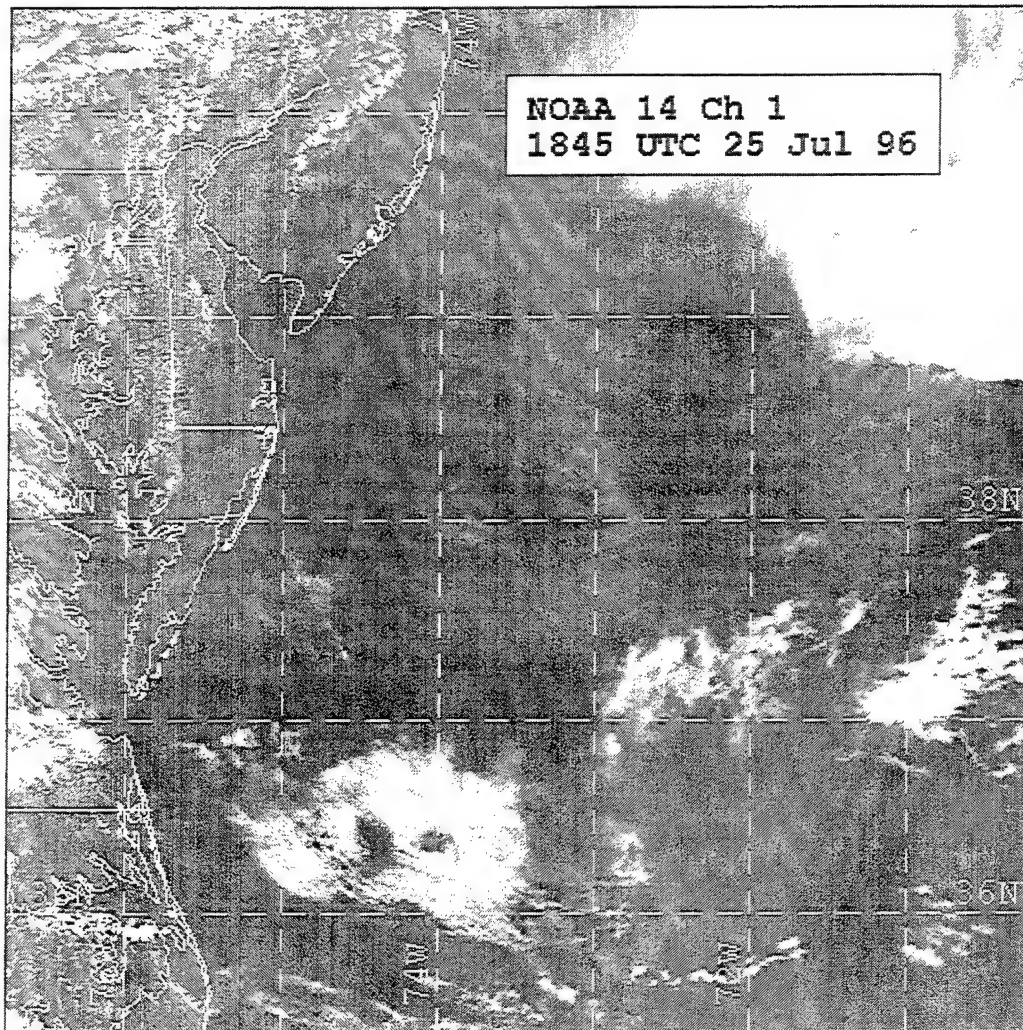


Figure 5.1. NOAA 14 AVHRR Channel 1 image of TARFOX Operating Area, 1842 UTC 25 July 1996.

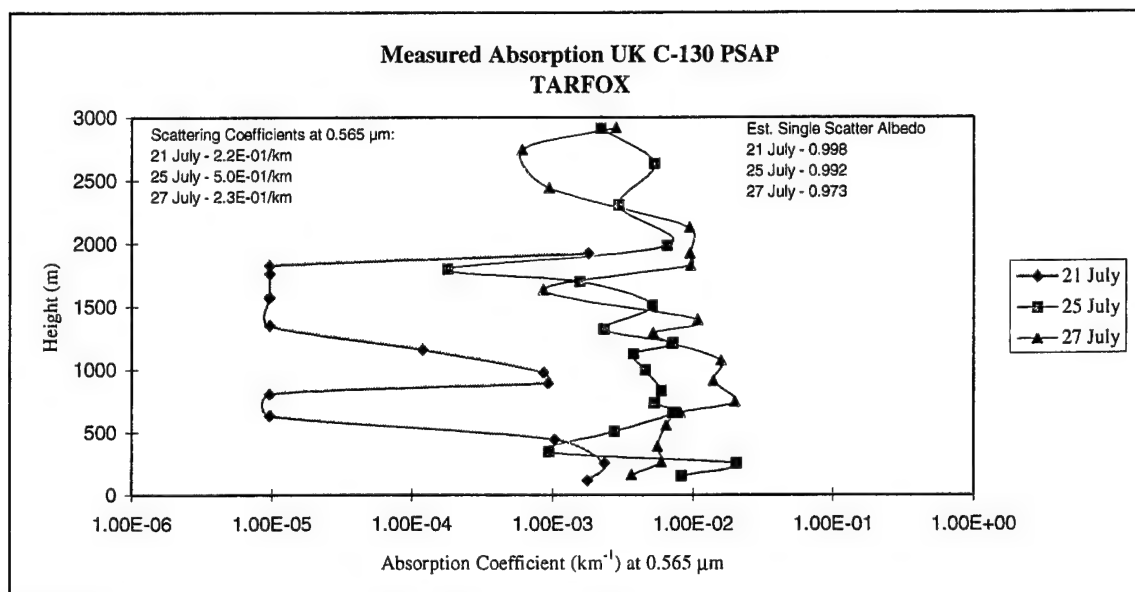


Figure 5.2. UK C-130 PSAP measured absorption coefficients at 0.565 μm for flights A466, A469, and A470. Scattering coefficients at 0.565 μm based on PCASP aerosol size distributions and resultant estimated single scattering albedos are included.

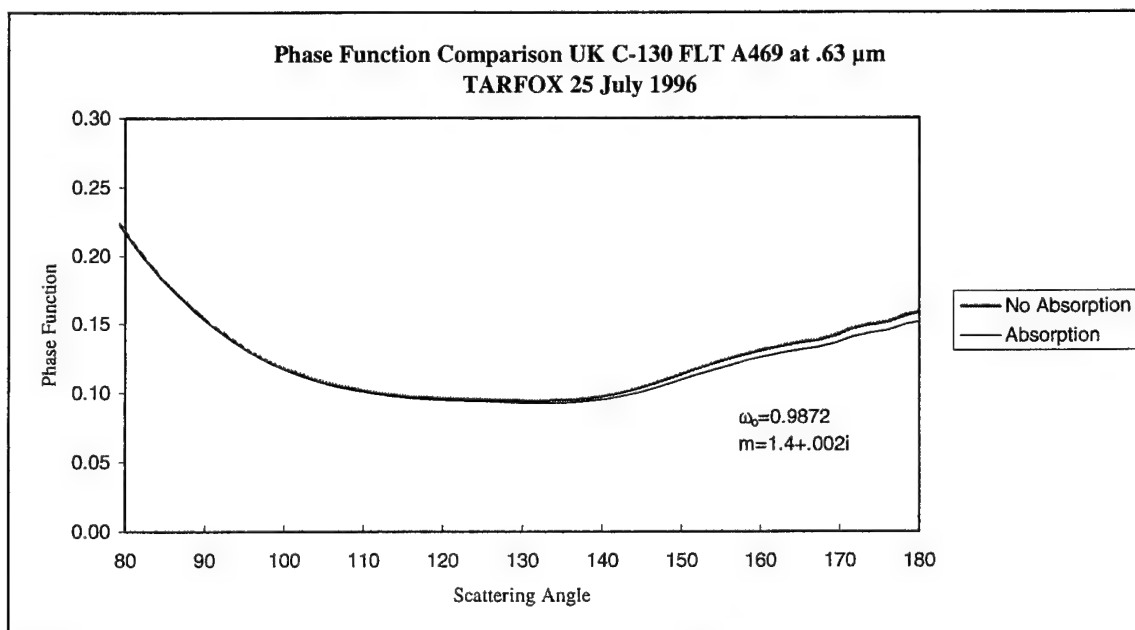


Figure 5.3. Comparison of Mie calculated phase functions for flight A469 PCASP measured size distributions with and without absorption. Absorption based on PSAP measured absorption coefficients.

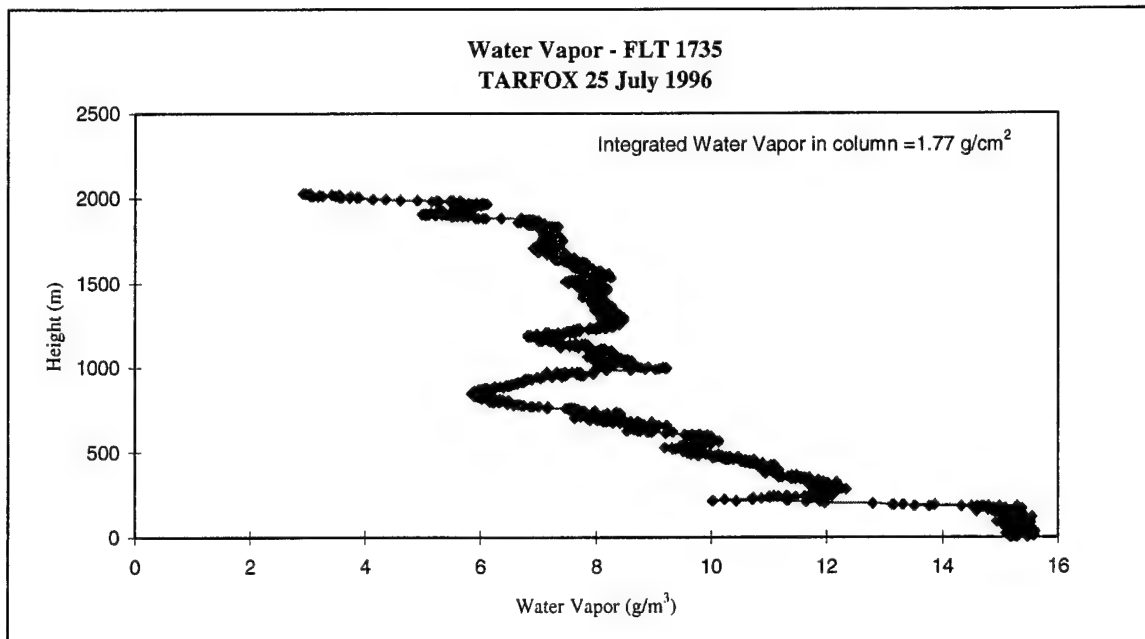


Figure 5.4. Column water vapor based on temperature and dew point measurements taken by University of Washington C-131A during flight 1735, 25 July 1996. Column integrated water vapor in 2 km layer is 1.77 g/cm^2 .

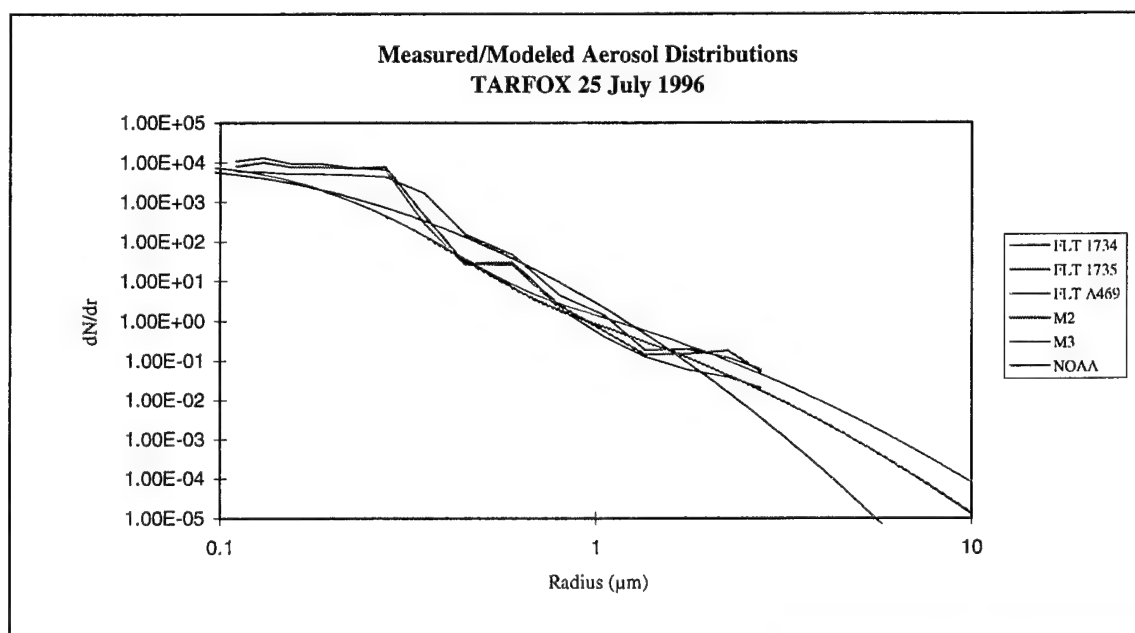


Figure 5.5. Comparison of PCASP measured aerosol size distributions (dN/dr) and model size distributions. Based on measured S_{12} values from NOAA AVHRR optical depth retrievals on 25 July 1996, algorithm estimated aerosol distributions were between M2 and M3 aerosol distribution models.

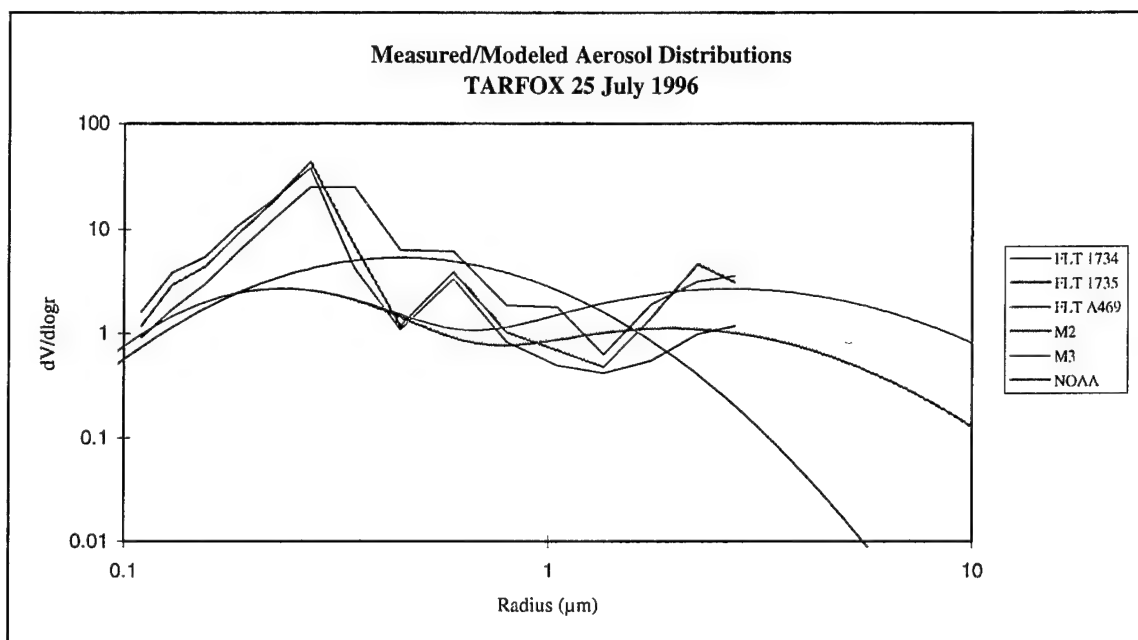


Figure 5.6. Comparison of PCASP measured aerosol size distributions ($dV/d\log r$) and model size distributions. Based on measured S_{12} values from NOAA AVHRR optical depth retrievals on 25 July 1996, algorithm estimated aerosol distributions were between M2 and M3 aerosol distribution models.

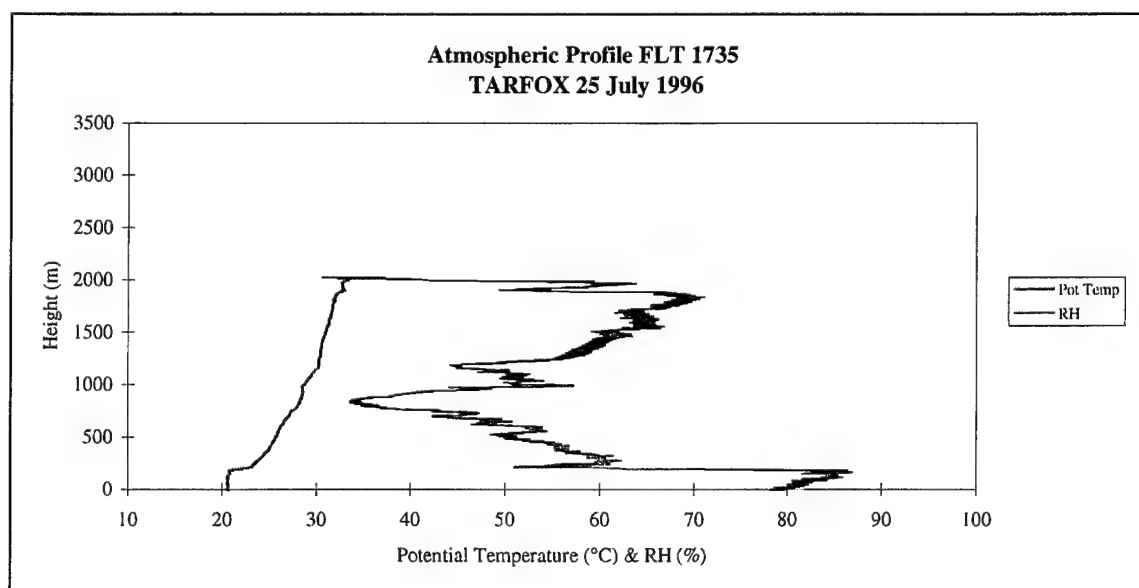


Figure 5.7. Lower atmospheric potential temperature and relative humidity (RH) profiles measured by University of Washington C-131A during flight 1735, 25 July 1996.

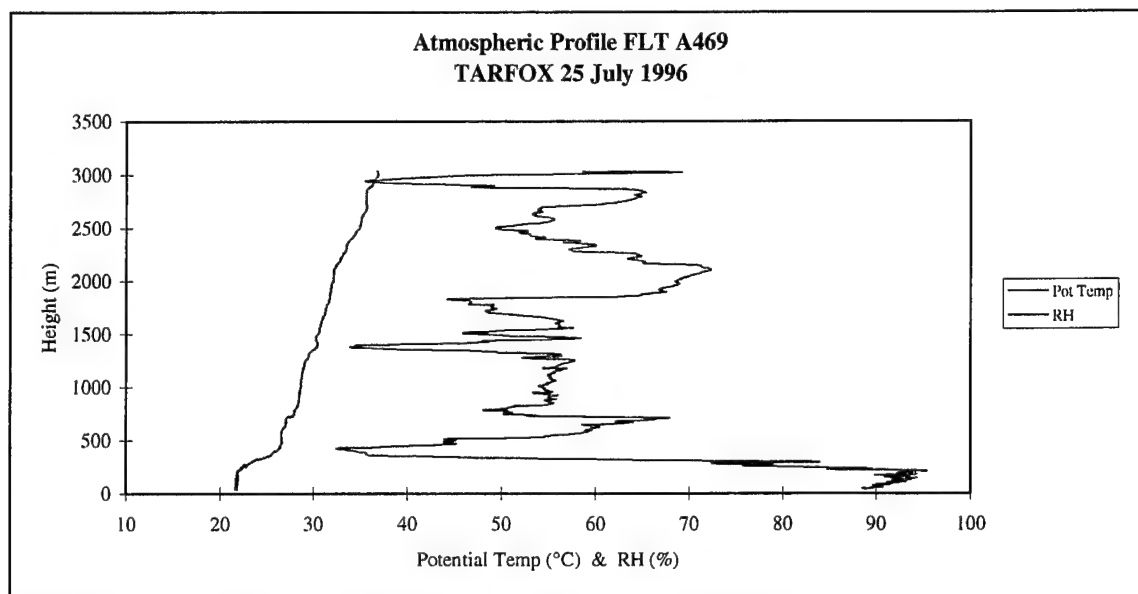


Figure 5.8. Lower atmospheric potential temperature and relative humidity (RH) profiles measured by UK C-130 during flight A469, 25 July 1996.

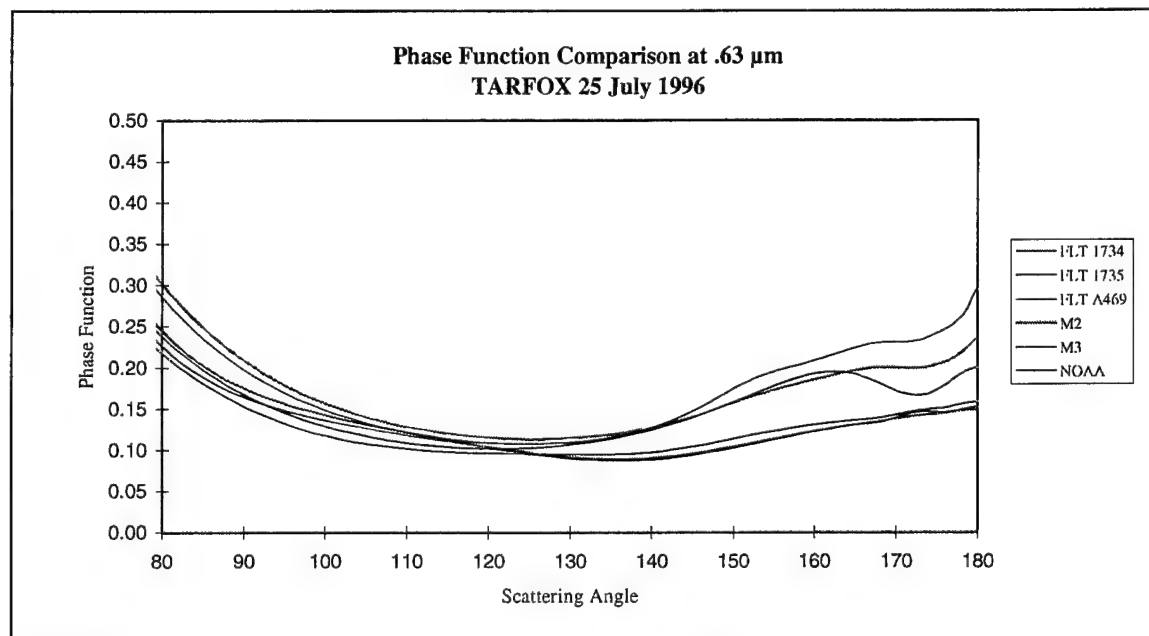


Figure 5.9. Comparison of Mie calculated phase functions at 0.63 μm based on PCASP aerosol size distributions measured during flights 1734, 1735, and A469 on 25 July 1996 and model aerosol distributions.

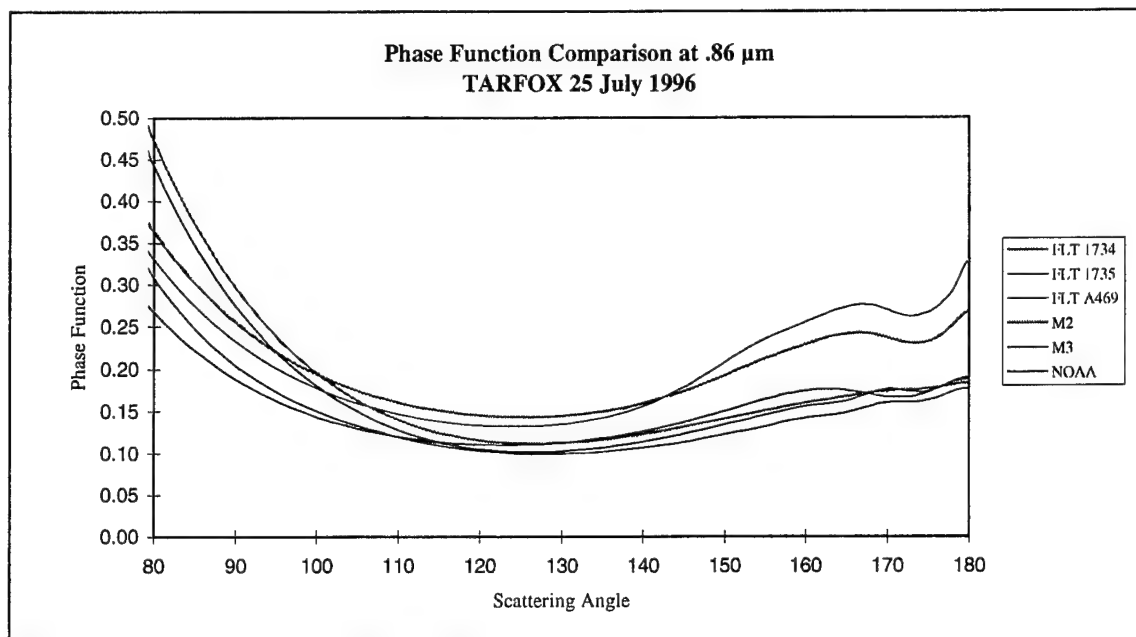


Figure 5.10. Comparison of Mie calculated phase functions at 0.86 μm based on PCASP aerosol size distributions measured during flights 1734, 1735, and A469 on 25 July 1996 and model aerosol distributions.

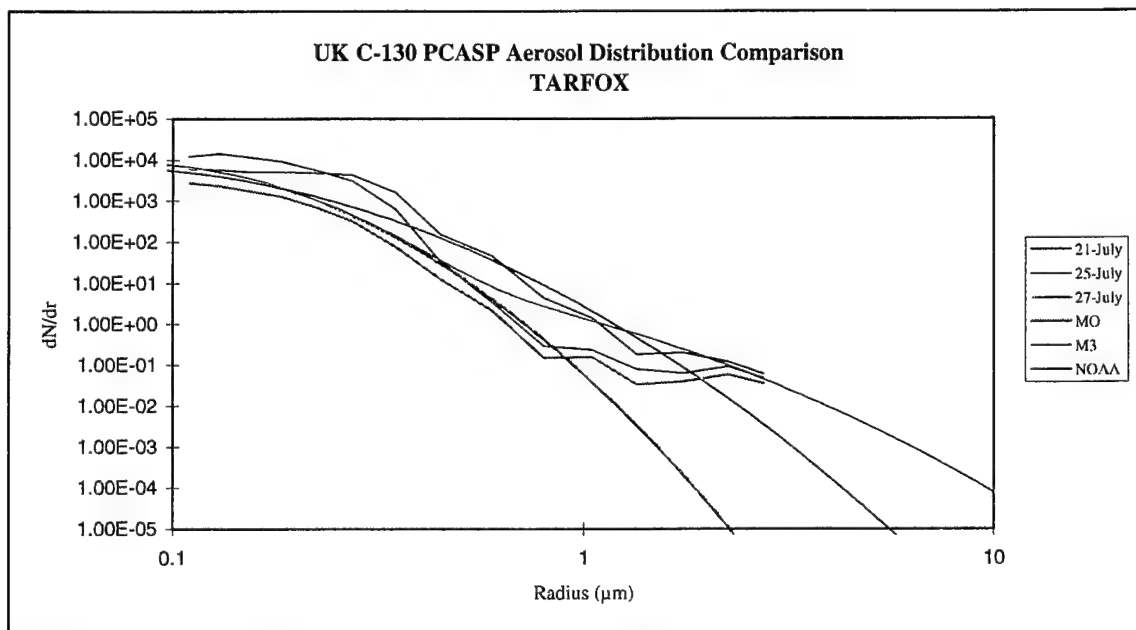


Figure 5.11. Comparison of UK C-130 PCASP measured aerosol size distributions (dN/dr) from flights A466, A469, A470 and model size distributions. Algorithm estimated distributions between M0 and M3.

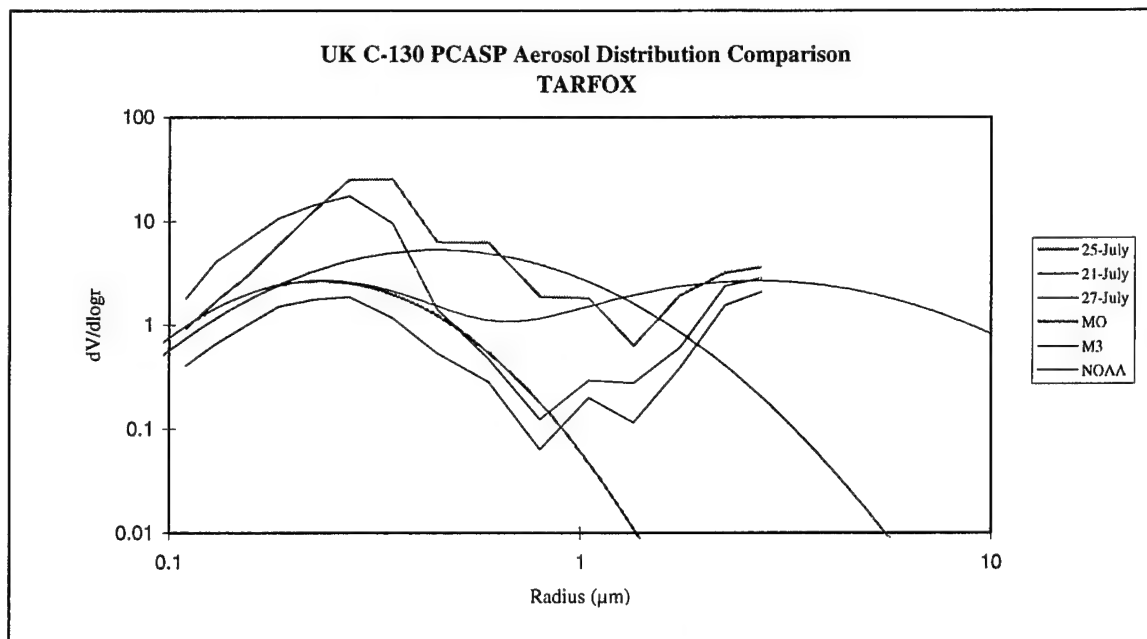


Figure 5.12. Comparison of UK C-130 PCASP measured aerosol size distributions ($dV/d\log r$) from flights A466, A469, A470 and model size distributions. Algorithm estimated distributions between M0 and M3.

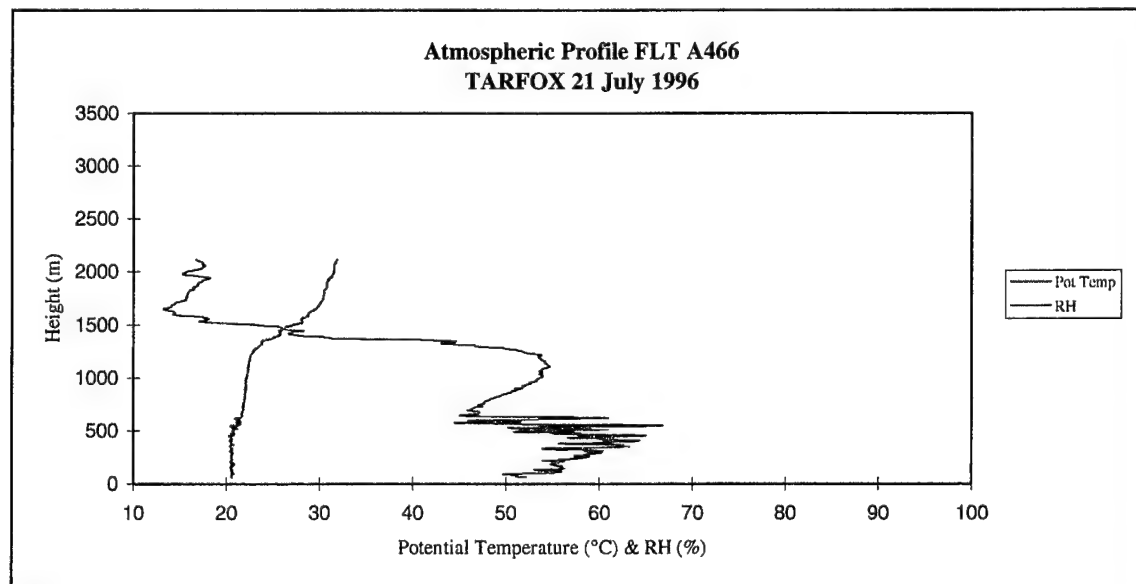


Figure 5.13. Lower atmospheric potential temperature and relative humidity (RH) profiles measured by UK C-130 during flight A466, 21 July 1996.

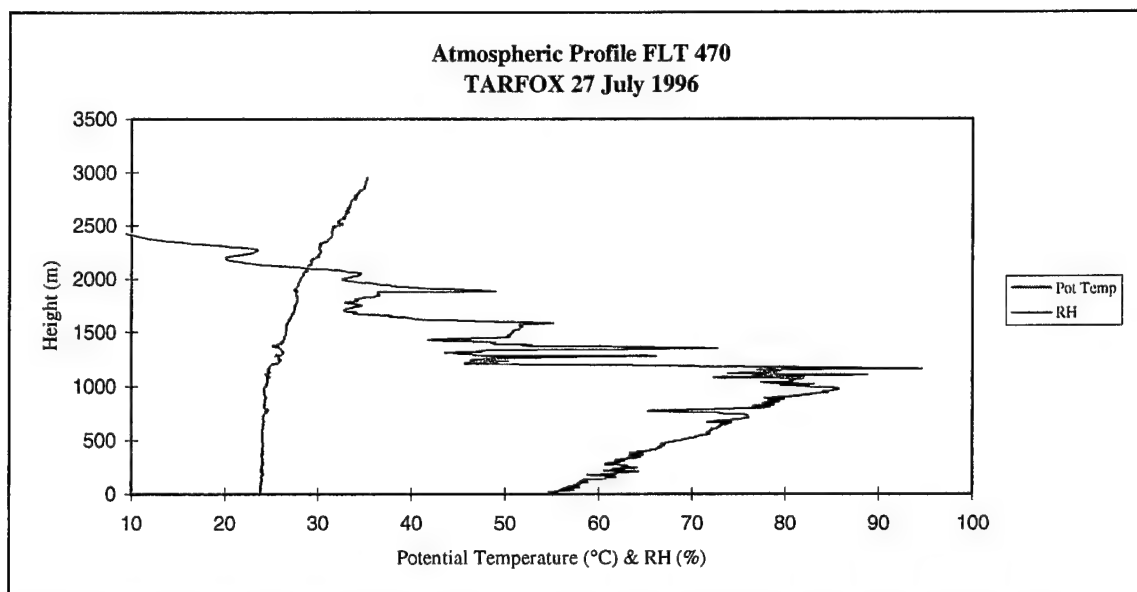


Figure 5.14. Lower atmospheric potential temperature and relative humidity (RH) profiles measured by UK C-130 during flight A470, 27 July 1996.

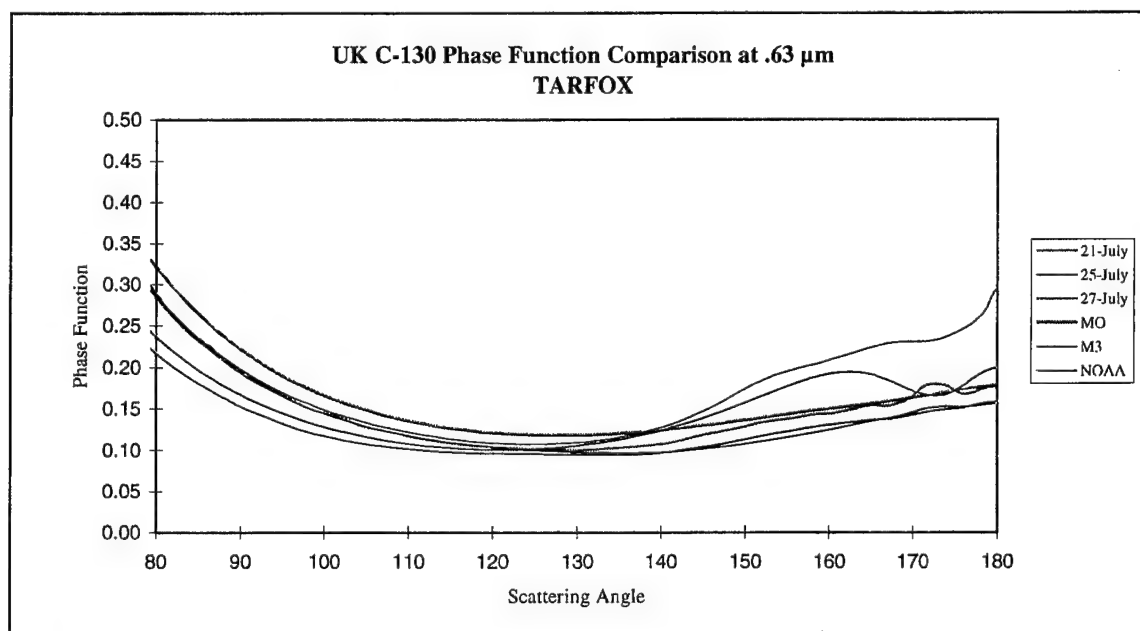


Figure 5.15. Comparison of Mie calculated phase functions at $0.63 \mu\text{m}$ based on PCASP aerosol size distributions measured during flights A466, A469, and A470 and model aerosol distributions.

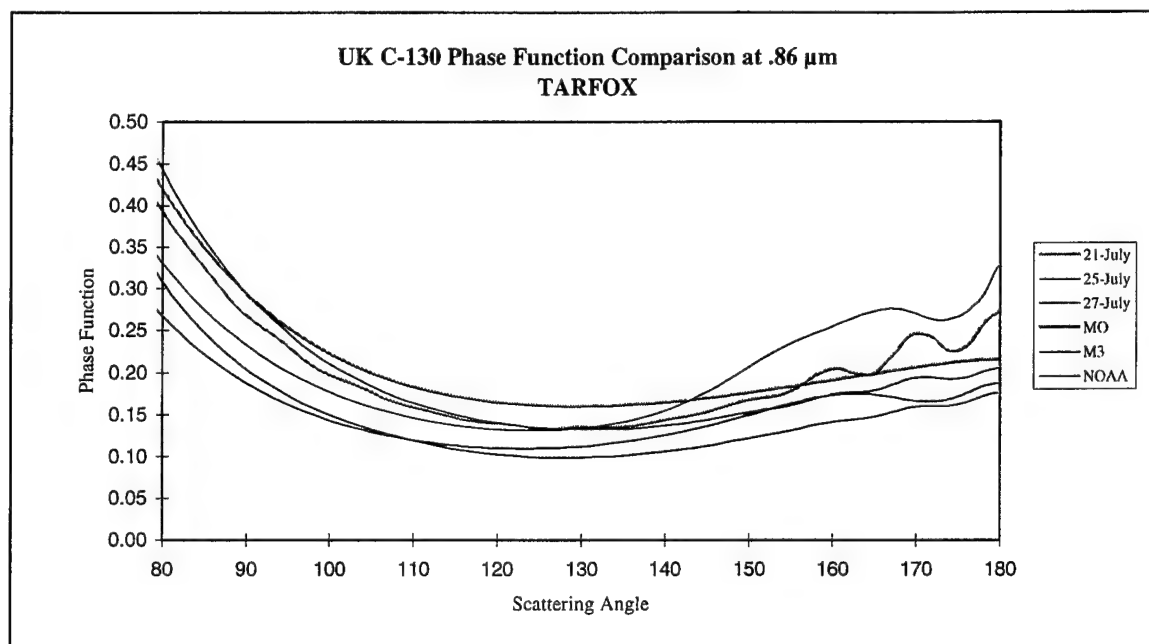


Figure 5.16. Comparison of Mie calculated phase functions at 0.86 μm based on PCASP aerosol size distributions measured during flights A466, A469, and A470 and model aerosol distributions.

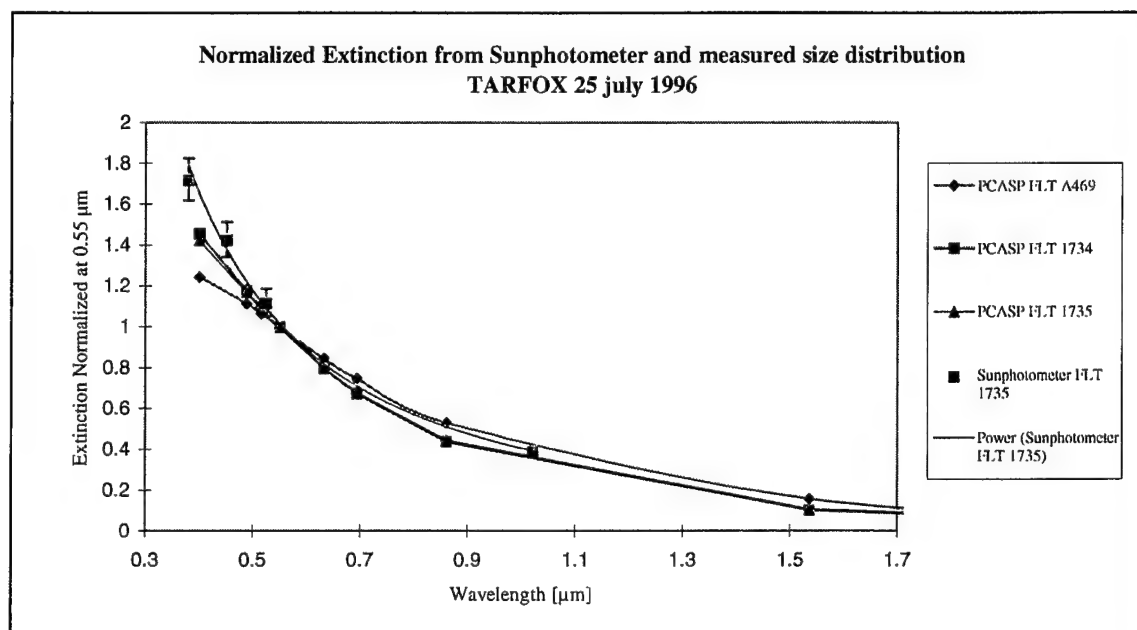


Figure 5.17. Comparison of extinction (normalized to 0.55 μm) measured by AMES sunphotometer and calculated from PCASP aerosol distributions, 25 July 1996.

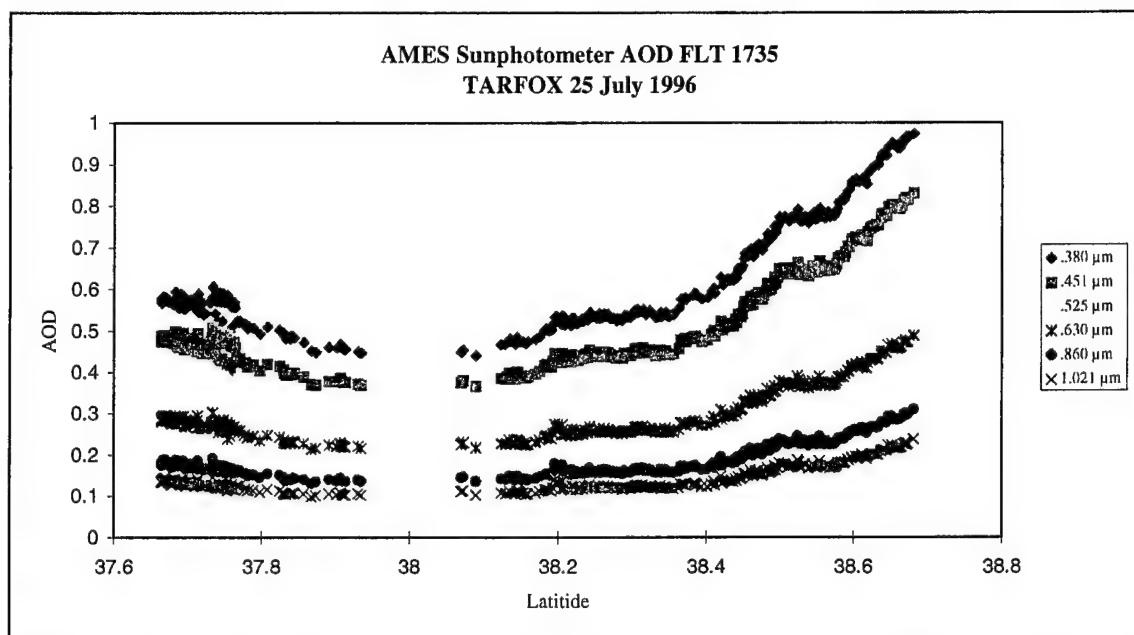


Figure 5.18. Measured aerosol optical depth (AOD) from AMES sunphotometer University of Washington C-131A flight 1735, 25 July 1996. Values at 0.63 μm and 0.86 μm computed using power law fit from values reported at 0.38 μm , 0.451 μm , 0.525 μm and 1.021 μm .

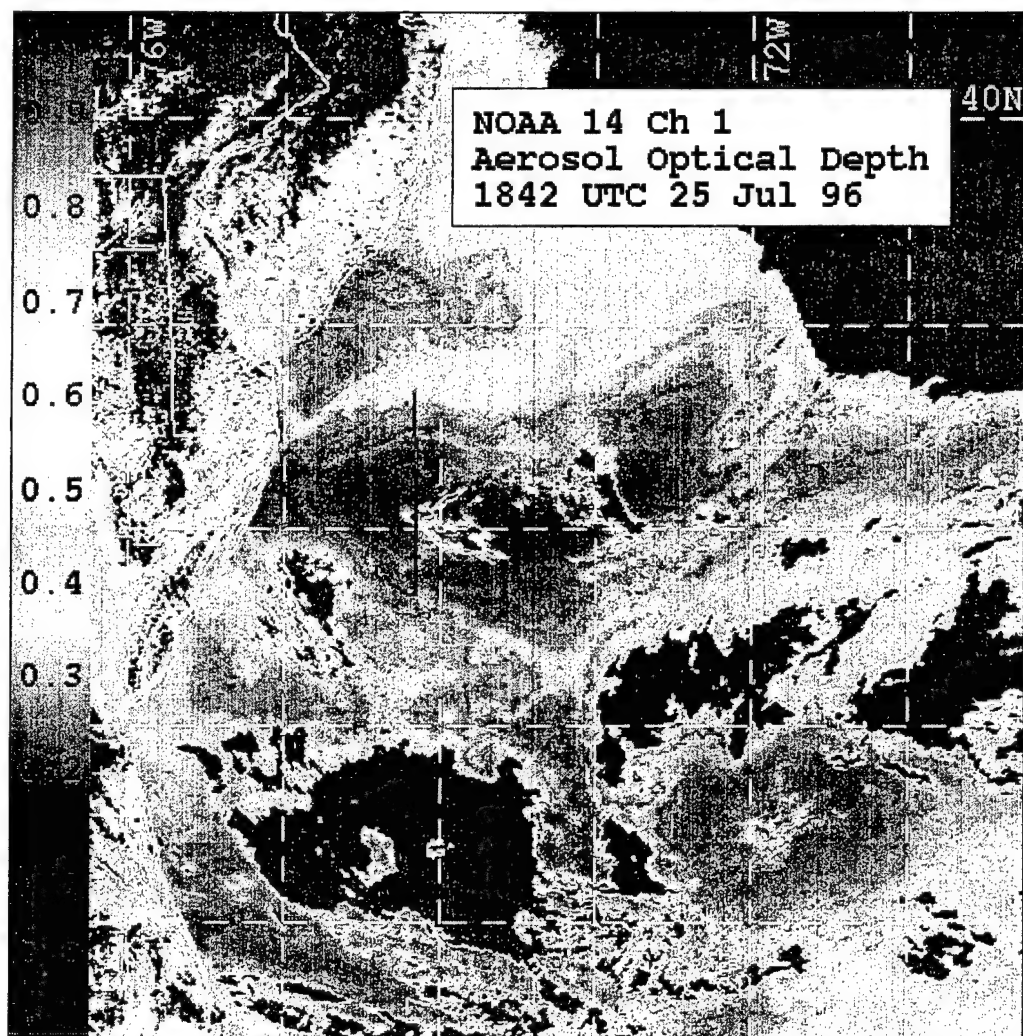


Figure 5.19. NOAA 14 retrieved aerosol optical depth at 0.63 μm , 1842 UTC 25 July 1996. Flight 1735 low level track annotated in red.

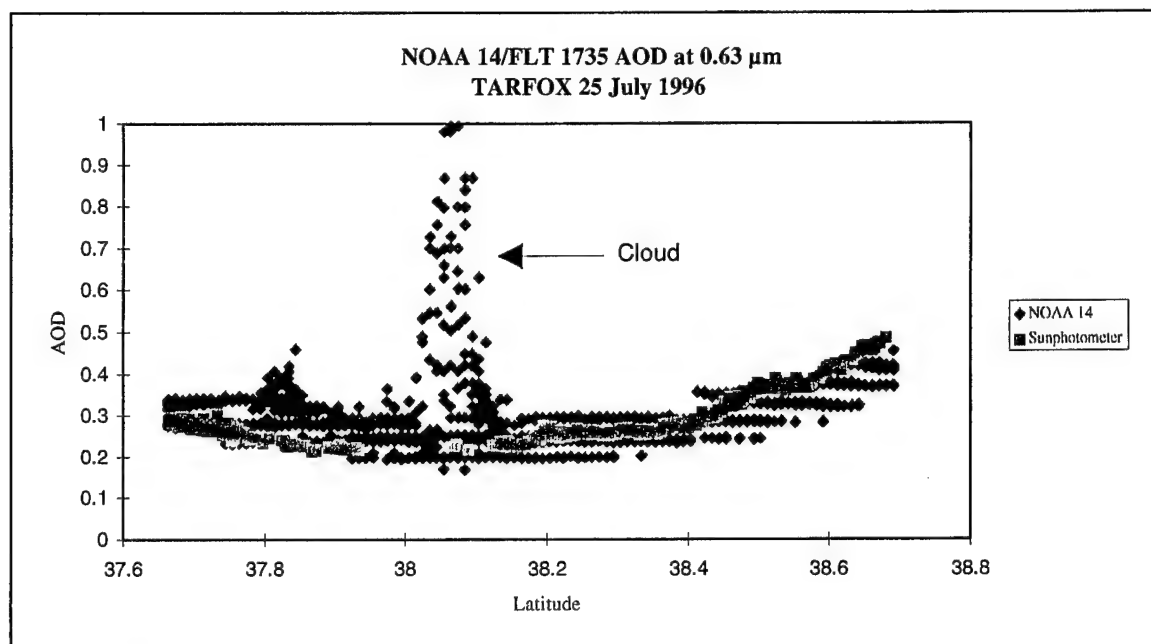


Figure 5.20. Comparison of aerosol optical depth (AOD) at 0.63 μm measured by AMES sunphotometer during flight 1735 and calculated by NOAA 14 retrieval algorithm using S_{12} phase function parameterization for 1842 UTC overpass, 25 July 1996.

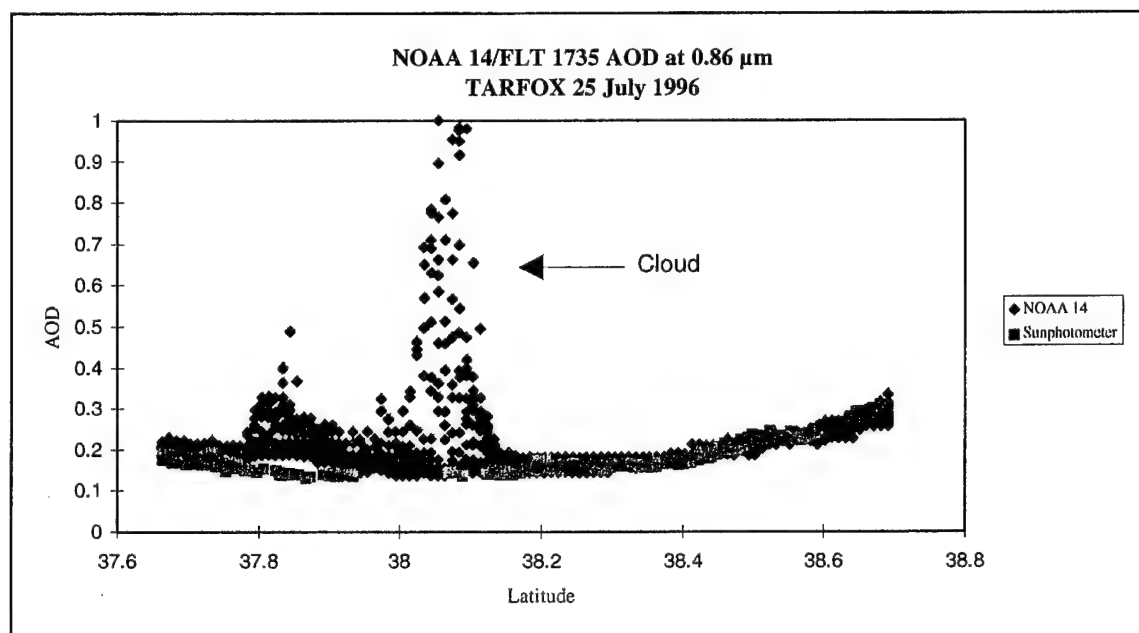


Figure 5.21. Comparison of aerosol optical depth (AOD) at 0.86 μm measured by AMES sunphotometer during flight 1735 and calculated by NOAA 14 retrieval algorithm using S_{12} phase function parameterization for 1842 UTC overpass, 25 July 1996.

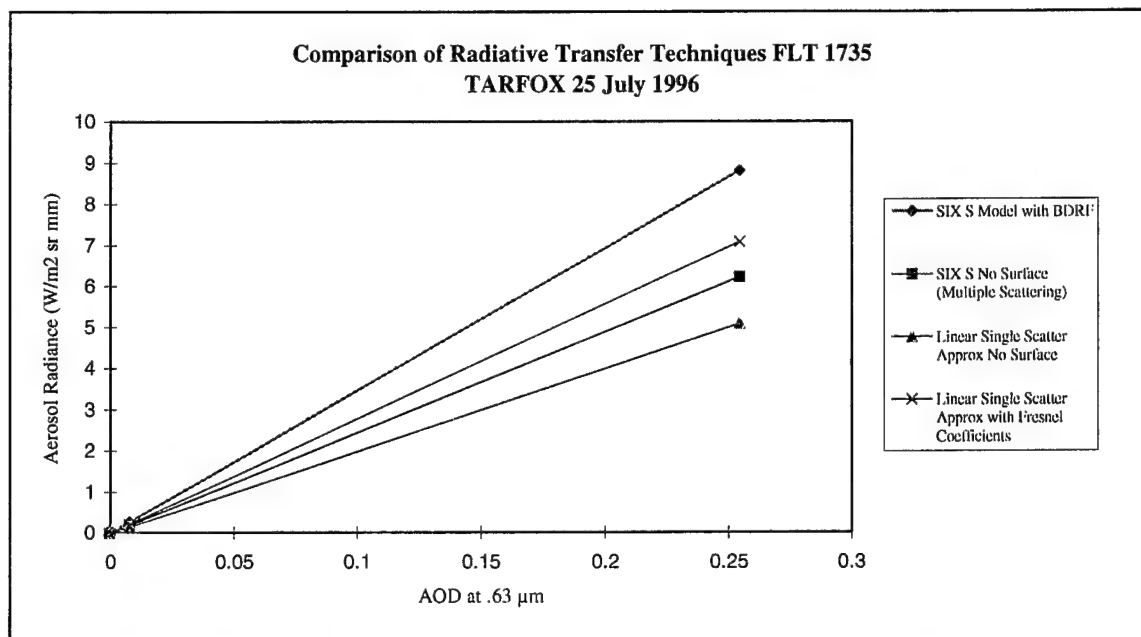


Figure 5.22. Comparison of radiative transfer techniques based on measured PCASP aerosol size distributions from flight 1735, 25 July 1996. The blue line represents the SIX S multiple-scattering, bi-directional specular surface model solution which is consistent with sunphotometer measurements during flight 1735. The remaining lines represent radiative transfer solutions for multiple-scattering without an underlying surface, linearized, single-scattering without an underlying surface, and the linearized, single-scattering algorithm used in this study. The slope of the lines are illustrative of the effective phase function. The largest error in radiative transfer solution using the study algorithm with a correct aerosol size distribution is due to the limitations of the algorithm's parameterization of reflectance off a specular ocean surface.

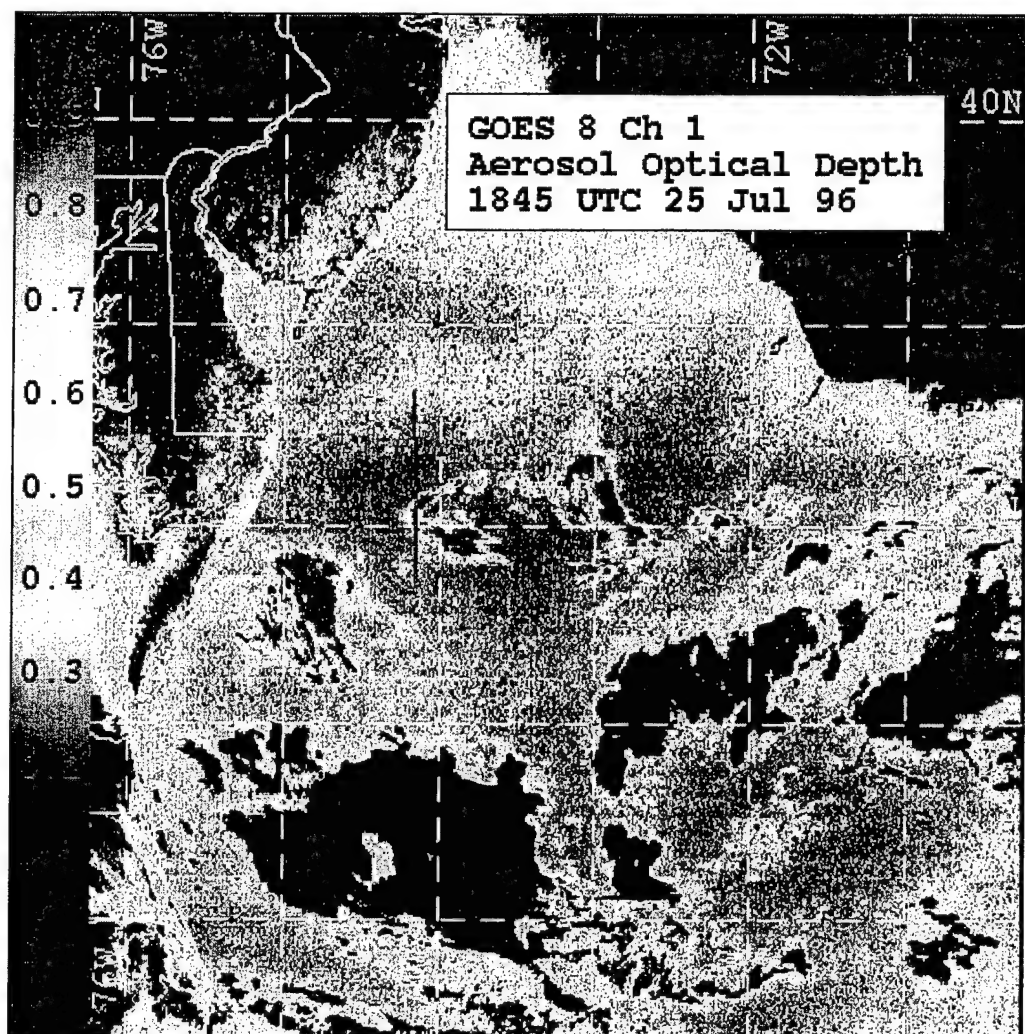


Figure 5.23. GOES 8 retrieved aerosol optical depth at 0.63 μm , 1845 UTC 25 July 1996. Flight 1735 low level track annotated in red.

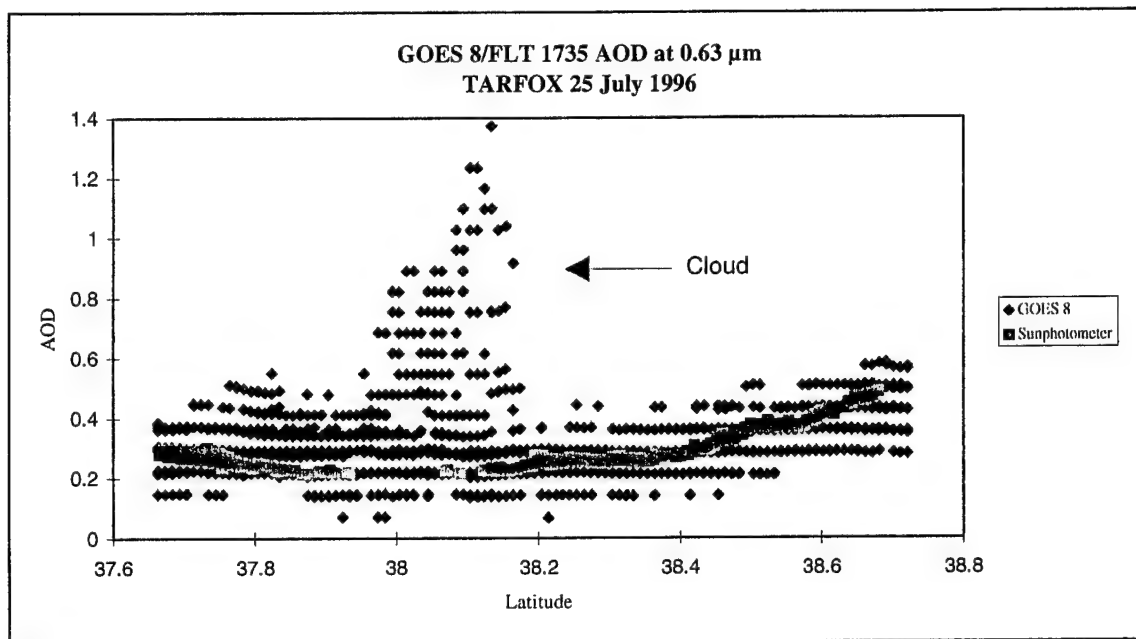


Figure 5.24. Comparison of aerosol optical depth (AOD) at 0.63 μm measured by AMES sunphotometer during flight 1735 and calculated by GOES retrieval algorithm using NOAA 14 S_{12} phase function parameterization for 1845 UTC overpass, 25 July 1996.

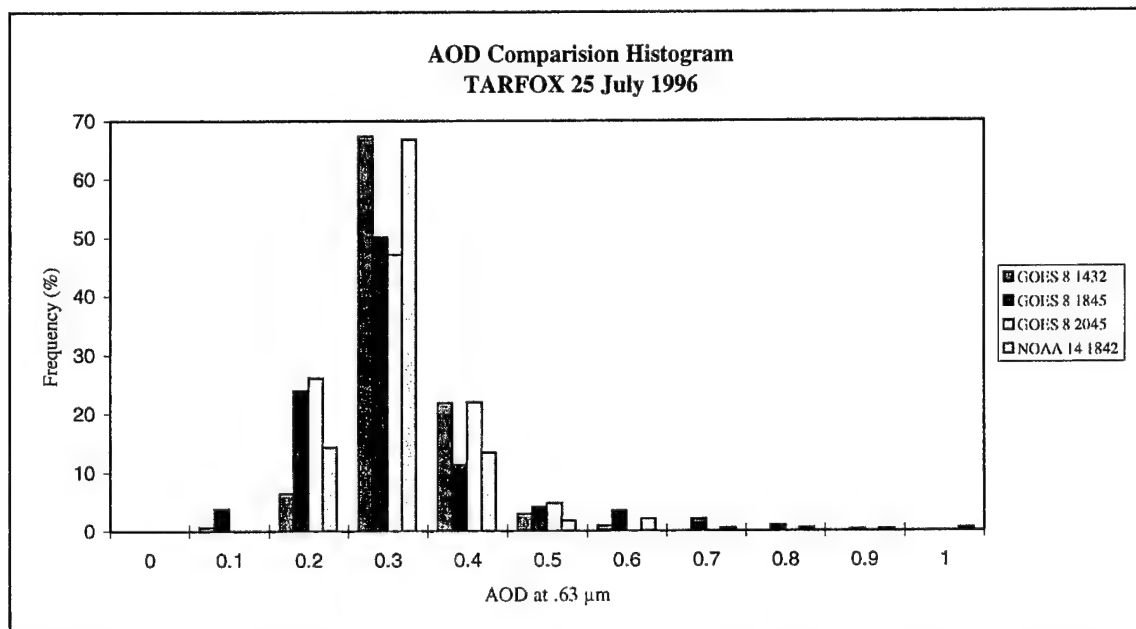


Figure 5.25. Comparison of satellite retrieved aerosol optical depth (AOD) at 0.63 μm for GOES 8 and NOAA 14 overpasses, 25 July 1996.

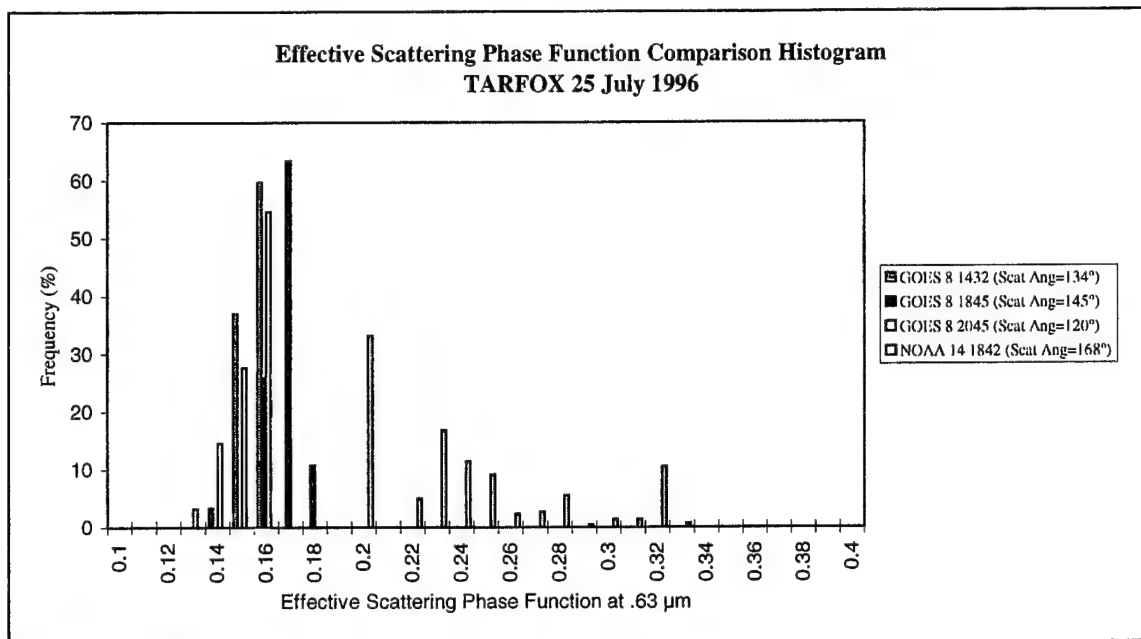


Figure 5.26. Comparison of algorithm computed effective phase function at 0.63 μm for GOES 8 and NOAA 14 overpasses, 25 July 1996.

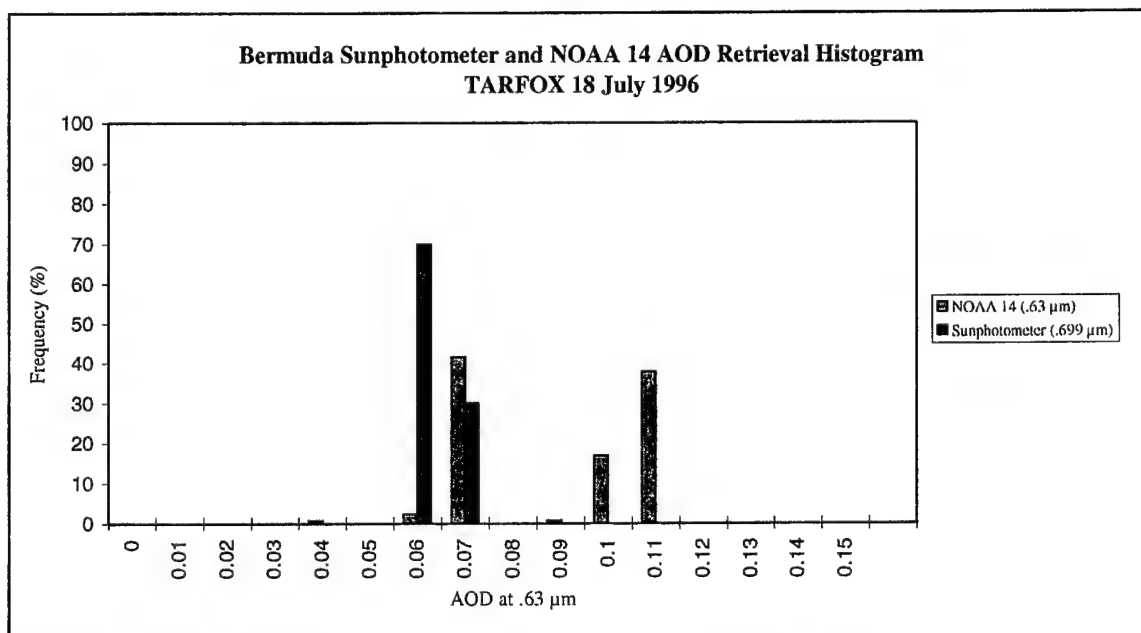


Figure 5.27. Comparison of aerosol optical depth (AOD) at 0.63 μm measured by Bermuda sunphotometer and NOAA 14 satellite retrieval, 18 July 1996.

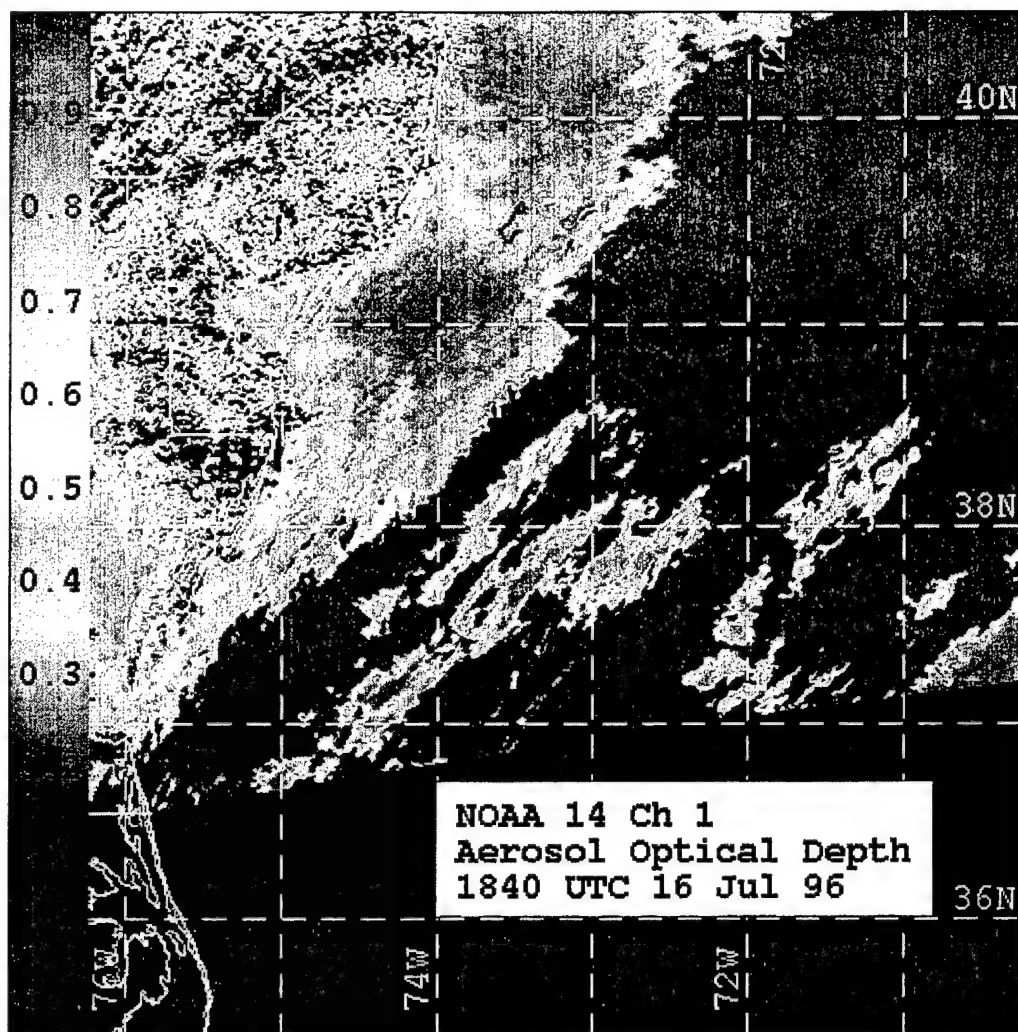


Figure 5.28. NOAA 14 retrieved aerosol optical depth, 1840 UTC 16 July 1996. Flight 1727 low level track annotated in red.

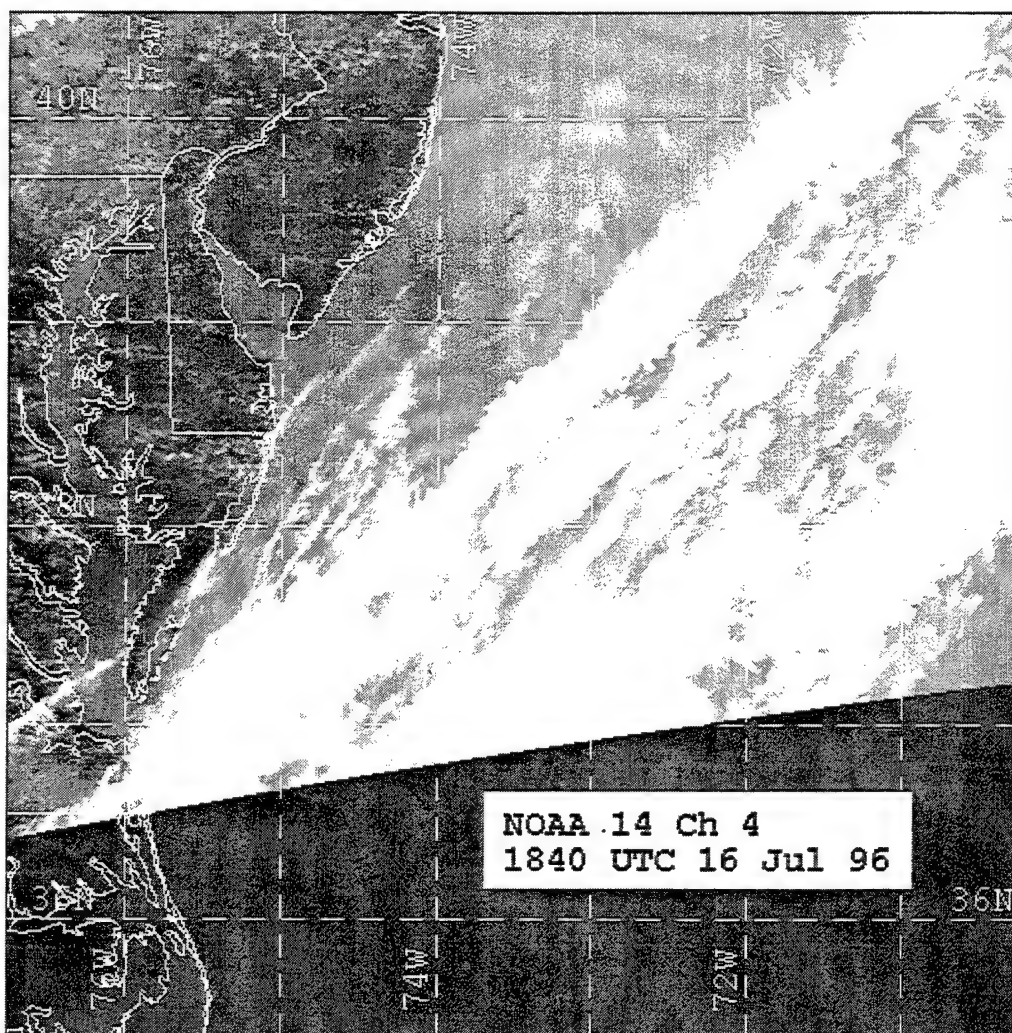


Figure 5.29. NOAA channel 4 image, 1840 UTC 16 July 1996. Flight 1727 low level track annotated in red. Note thin cirrus shield over flight track.

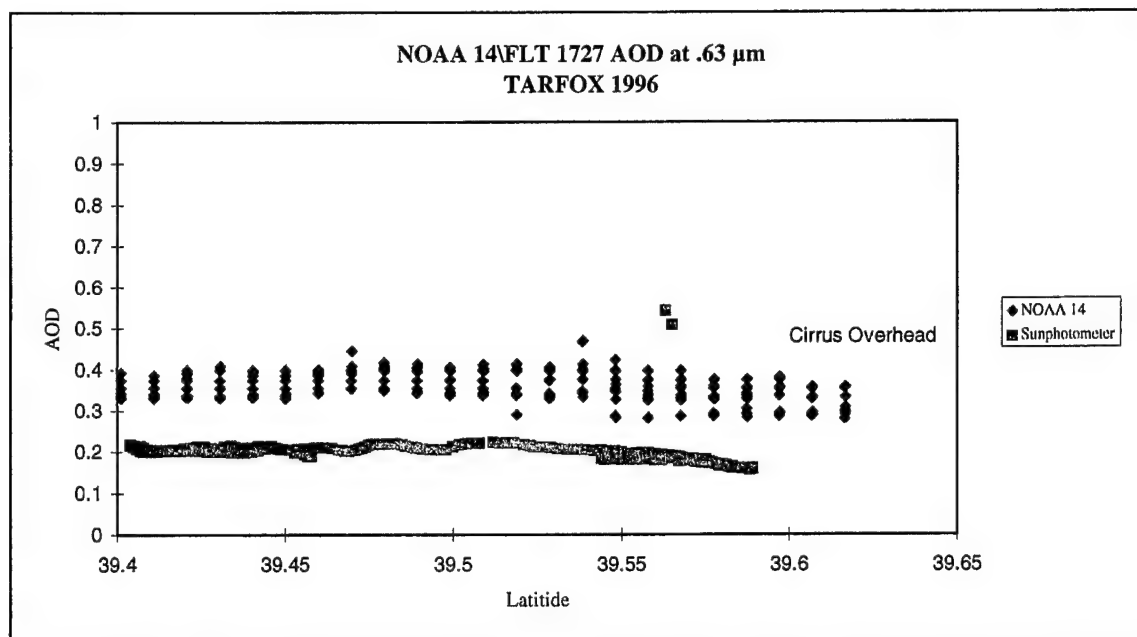


Figure 5.30. Comparison of aerosol optical depth (AOD) at 0.63 μm measured by AMES sunphotometer during flight 1727 and calculated by NOAA 14 retrieval algorithm using S_{12} phase function parameterization for 1840 UTC overpass, 16 July 1996.

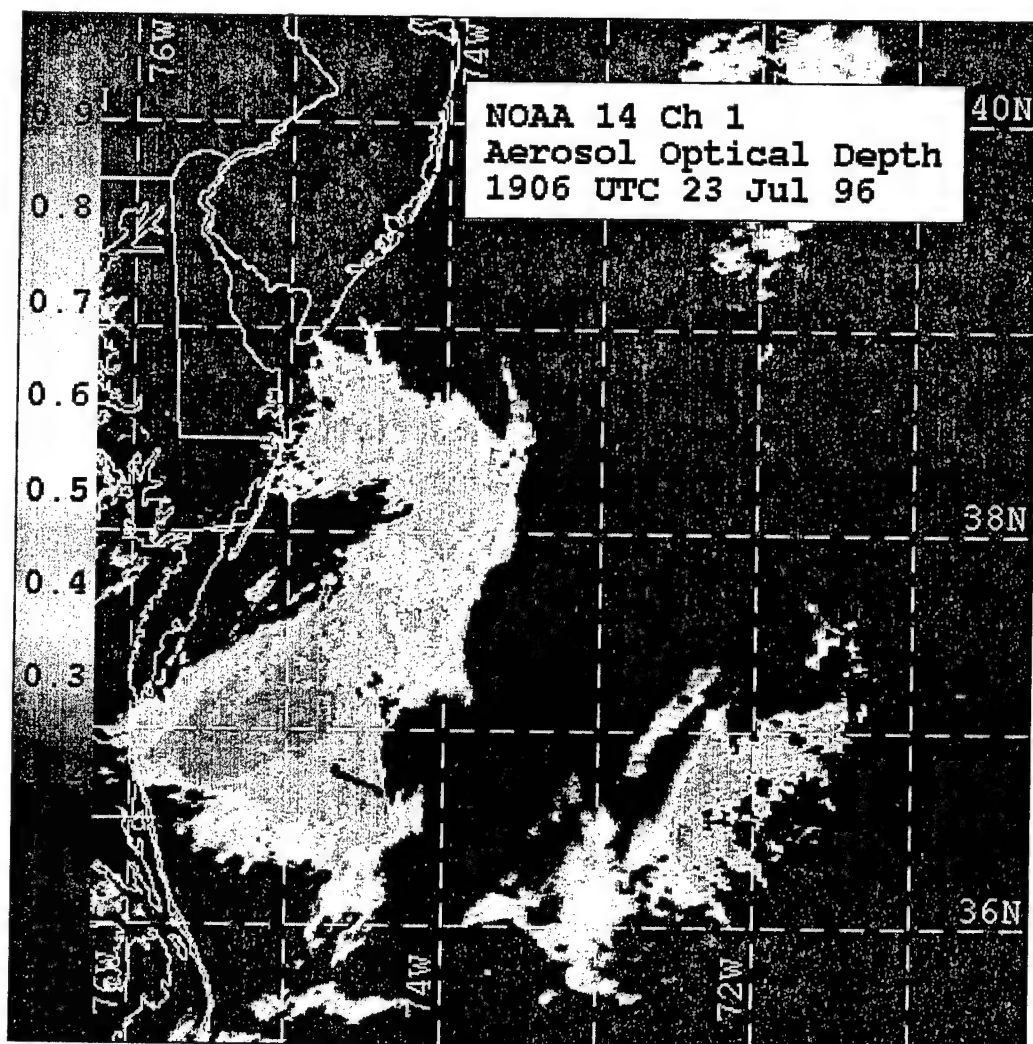


Figure 5.31. NOAA 14 retrieved aerosol optical depth, 1906 UTC 23 July 1996. Flight 1732 low level track annotated in red.

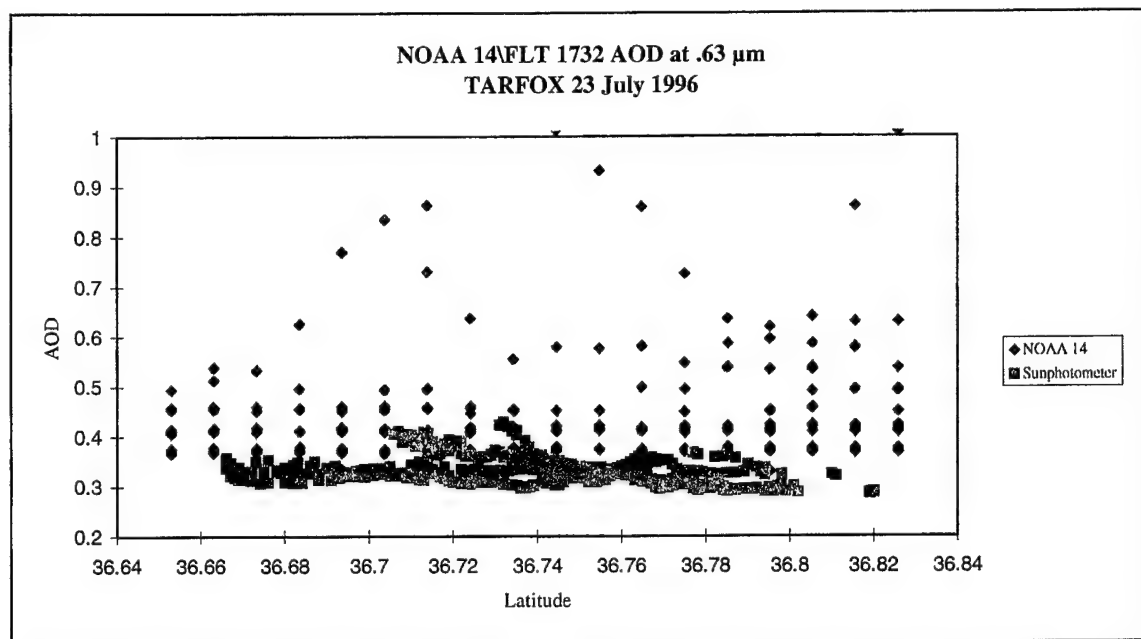


Figure 5.32. Comparison of aerosol optical depth (AOD) at 0.63 μm measured by AMES sunphotometer during flight 1732 and calculated by NOAA 14 retrieval algorithm using S_{12} phase function parameterization for 1904 UTC overpass, 23 July 1996.

VI. CONCLUSIONS/RECOMMENDATIONS

A. CONCLUSIONS

A linearized, single scattering satellite aerosol optical depth algorithm with a spectral surface reflectance approximation was presented for the NOAA POES AVHRR and GOES Imager. Comparison of satellite derived aerosol optical depths with *in situ* data collected during TARFOX indicate some errors in the retrieval algorithm which are explored. Despite these errors, application of the AVHRR phase function parameterization to the GOES Imager retrievals produces temporarily consistent aerosol optical depth values which promotes the potential of the GOES instrument for aerosol optical depth studies.

Lack of more than one day of complete closure data due to weather during TARFOX and access constraints to post experiment data limited the scope of validation of satellite aerosol optical depth retrieval procedures outlined in this thesis. With the data available, several notable findings and shortcomings of the retrieval method were discovered.

The linearized, single-scattering satellite aerosol optical depth retrieval algorithm designed and tested using NOAA 14 and GOES 8 imagery during TARFOX showed some skill at measuring aerosol optical depth as measured by the AMES sunphotometer. In particular, retrieval of radiance due to aerosol scatter appears to correlate well with that calculated by the SIX S model, suggesting that treatment of ozone absorption, Rayleigh scatter, and surface reflectance within the assumptions in the model is satisfactory.

The largest errors in the model are related to the lack of skill in modeling expected aerosol distributions to parameterize the phase functions. Both the NOAA/NESDIS and study model distributions differed significantly from PCASP

measured size distributions in the TARFOX area. These deviations resulted in phase function errors of roughly 20-40%.

Based on the linearity of the retrieval method, satellite derived aerosol optical depths should have shown errors of comparable magnitude. However, the results of the retrievals showed good fit with sunphotometer data. Comparison of this retrieval technique with the SIX S multiple scattering, bi-directional reflectance model (which consistently calculated observed aerosol optical depth given the Sun-Earth-satellite geometry and observed aerosol size distribution) appear to indicate that lack of skill in treatment of bi-directional surface reflectance and lack of multiple scattering in the study linear single scatter model may have created an offsetting error to the phase function.

Despite these limitations in the linear single scattering retrieval, consistency in error was observed over the course of several days in the AVHRR data between cases of relatively high and low optical depths. The retrievals show that the resolution of aerosol optical depth retrieved by the AVHRR is approximately 0.04 due to the limitations of digitization in channel 1 and 2 in low optical depth environments. The AVHRR data also illustrates sensitivity to retrievals with inadequate cloud screening, especially for thin cirrus, and retrievals near cloud boundaries which would need to be addressed further in applying the retrieval operationally.

Extension of the S_{12} phase function parameterization to the GOES 8 yielded good consistency with the AVHRR retrieved optical depths for the one day analyzed. From the data retrieved, the resolution of GOES Imager aerosol optical depth appears to be more limited than the AVHRR, on the order of 0.7.

From PCASP data, aerosol loading in the TARFOX area remained fairly homogeneous over the course of 25 July 1996. The GOES retrieval algorithm demonstrated skill at applying the 1842 UTC NOAA S_{12} phase function parameterization both forward and backward in time over several hours. It appears feasible to parameterize the GOES phase function using data obtained from the AVHRR. However, it is expected that degradation of the AVHRR derived phase function information with time will occur due to variability of aerosol loading in the environment. The limitations of the application of AVHRR derived phase functions to GOES has not been adequately defined.

B. RECOMMENDATIONS

As a result of this study, the following recommendations are suggested:

- Obtain remainder of PCASP data collected by UW C-131A for inclusion into this study.

- Implement further closure studies in other locations to completely test model aerosol distributions and phase function parameterization.

- Conduct in-depth analysis into the errors assumed in the linear single scatter model in reference to bi-directional reflectance. Quantify tradeoffs between a linear single scatter model and multiple scattering, bi-directional lookup table techniques. Study the possibility of parameterizing bi-directional reflectance in the linear single scattering model with minimal error.

- Extend the S_{12} phase function parameterization technique to next generation AVHRR with 1.6 μm daytime channel (less sensitive to water vapor than channel 2).

- Further test the sensitivity of GOES retrieval to S_{12} phase function parameterization. Determine limits of application through larger data set.

- Apply retrieval technique to west coast of United States using NOAA 14 and GOES 9.

- Explore the possibility of estimating aerosol distributions based on shift of scattering angle over time with GOES retrieved aerosol optical depth data.

LIST OF REFERENCES

- Charlson, R. J., , S. E. Swartz, J. M. Hales, R. D. Cess, J. A. Coakley, Jr., J. E. Hansen and D. J. Hoffman (1992). Climate forcing by anthropogenic aerosols. *Science*, **255**, 423-430.
- Dalu, G. (1986). Satellite remote sensing of atmospheric water vapor. *International Journal of Remote Sensing*, **7**, 1089-1097.
- Durkee, P. A., F. Pfeil, E. Frost and R. Shema (1991). Global analysis of aerosol particle characteristics. *Atmos. Env.*, **25A**, 2457-2471.
- Elterman, L. (1970). Vertical-attenuation model with eight surface meteorological ranges 2 to 13 kilometers. AFCRL-70-0200 Air Force Cambridge Research Laboratory, Cambridge, MA, 56pp.
- GOES-IJ/KLM SN03 Imager Data and Calibration Handbook. Space Systems/Loral, Palo Alto, CA. ITT Aerospace/Communications Division (1994).
- GOES Calibration and Alignment Handbook for the Imager SN04 Instrument. Space Systems/Loral, Palo Alto, CA. ITT Aerospace/Communications Division (1994).
- Gordon, H. R. and D. K. Clark (1980). Atmospheric effects in the remote sensing of phytoplankton pigments. *Boundary Layer Meteorology*, **18**, 299-313.
- Ignatov, A. M., L. L. Stowe, S. M. Sakerin and G. K. Korataev (1995). Validation of the NOAA/NESDIS satellite aerosol product over the North Atlantic in 1989. *J. Geophys. Res.*, **100**, 5123-5132.
- Kidwell, K. B. (1995). NOAA Polar Orbiter Data Users Guide. National Environmental Satellite, Data, and Information Service (NESDIS), National Oceanic and Atmospheric Administration, 394pp.
- Koepke, P. (1984). Effective reflectance of ocean whitecaps. *Appl. Opt.*, **23**, 1816-1824.
- Liou, K. N. (1980). *An Introduction to Atmospheric Radiation*. Academic Press, New York, 392pp.

- Mahony, T. P. (1991). Water vapor influence on satellite-measured aerosol characteristics. M.S. Thesis, Naval Postgraduate School, Monterey, CA, 43pp.
- Matsumoto, Y., C. Minä, P. B. Russell, and W. B. Vanark (1987). *Airborne tracking sunphotometer apparatus and system*. NASA Technical Report 1988005110 N (88N14492), NASA Ames Research Center, Moffett Field, CA, 10pp.
- Particle Soot/Absorption Photometer (PSAP) Operation Procedures*. Radiance Research, Seattle, WA, 9pp.
- Passive Cavity Aerosol Spectrometer Probe (Airborne) PMS Model PCASP-100X 0.10 - 3.0 mm Operating Manual*. Particle Measuring Systems, Inc., Boulder, CO, 40pp.
- Ramsey, R. C. (1968). *Study of the Remote Measurement of Ocean Color*. Final Report, TRW, NASW-1658, 94pp.
- Rao, C. R. N. and J. Chen (1995). Inter-satellite calibration linkages for the visible channels of the Advanced Very High Resolution Radiometer on the NOAA-7, -9, and -11. *International Journal of Remote Sensing*, 16, 1931-1942.
- Rouault, M. and P. A. Durkee (1992). Characterization of aerosols from satellite remote sensing. In *Nucleation and Atmospheric Aerosols*, 357-360, N. Fukuta and P. E. Wagoner (Eds.), A. Deepak Publishing.
- Russell, P.B., W. Whiting, P. V. Hobbs and L. L. Stowe (1996). *Tropospheric Aerosol Radiative Forcing Observational Experiment (TARFOX) Science and Implementation Plan*. NASA Ames Research Center, Moffett Field, CA, 50pp.
- Turner, R. (1973). Atmospheric effects in remote sensing. In *Remote Sensing of the Earth Resources, II*, 549-583, F. Shahrocki (ed.), University of Tennessee.
- Vermote, E., D. Tanré, J. L. Deuzé, M. Herman and J. J. Morcrette (1995). *Second Simulation of Satellite Signal in the Solar Spectrum (6S) Users Guide, Version 1*, 216pp.
- Whiting, W., P. B. Russell, P. V. Hobbs and L. L. Stowe (1996). *Tropospheric Aerosol Radiative Forcing Observational Experiment (TARFOX) Operations Summary*. International Global Atmospheric Chemistry Project (IGAC), 127pp.

INITIAL DISTRIBUTION LIST

	No. Copies
1. Defense Technical Information Center 8725 John J. Kingman Road, Ste 0944 Ft. Belvoir, Virginia 22060-6218	2
2. Dudley Knox Library Naval Postgraduate School 411 Dyer Rd. Monterey, California 93943-5101	2
3. Chairman, Code MR Department of Meteorology Naval Postgraduate School Monterey, California 93943-5002	4
4. Professor Philip A. Durkee (Code MR/DE) Department of Meteorology Naval Postgraduate School Monterey, California 93943-5002	4
5. J. Pepijn Veefkind Maasstraat P-C NL-3016 DC Rotterdam The Netherlands	1
6. LCDR Brian B. Brown Carrier Group Eight Unit 60104 FPO AE 09501-4308	2